Simplified Micro-Modeling of a Masonry Cross-Vault for Seismic Assessment Using the Distinct Element Method

Oktiovan, Y.P.; Davis, L.; Wilson, R.; Dell'Endice, A.; Mehrotra, A.; Pulatsu, B.; Malomo, D.

DOI
10.1080/15583058.2023.2277328

Publication date
2023

Document Version
Final published version

Published in
International Journal of Architectural Heritage

International Journal of Architectural Heritage
Conservation, Analysis, and Restoration

ISSN: (Print) (Online) Journal homepage: https://www.tandfonline.com/loi/uarc20

Simplified Micro-Modeling of a Masonry Cross-Vault for Seismic Assessment Using the Distinct Element Method

Y.P. Oktiovan, L. Davis, R. Wilson, A. Dell'Endice, A. Mehrotra, B. Pulatsu & D. Malomo

To cite this article: Y.P. Oktiovan, L. Davis, R. Wilson, A. Dell'Endice, A. Mehrotra, B. Pulatsu & D. Malomo (09 Nov 2023): Simplified Micro-Modeling of a Masonry Cross-Vault for Seismic Assessment Using the Distinct Element Method, International Journal of Architectural Heritage, DOI: 10.1080/15583058.2023.2277328

To link to this article: https://doi.org/10.1080/15583058.2023.2277328

Published online: 09 Nov 2023.

INTERNATIONAL JOURNAL OF ARCHITECTURAL HERITAGE
https://doi.org/10.1080/15583058.2023.2277328

Taylor & Francis
Taylor & Francis Group

RESEARCH ARTICLE

OPEN ACCESS Check for updates

Simplified Micro-Modeling of a Masonry Cross-Vault for Seismic Assessment Using the Distinct Element Method

Y.P. Oktiovan [a], L. Davis [b], R. Wilson [c], A. Dell'Endice [d], A. Mehrotra [a], B. Pulatsu [c], and D. Malomo [b]

[a]Faculty of Civil Engineering and Geosciences, Delft University of Technology, Delft, Netherlands; [b]Department of Civil Engineering, McGill University, Montreal, Canada; [c]Department of Civil and Environmental Engineering, Carleton University, Ottawa, Canada; [d]Institute of Technology in Architecture, ETH Zurich, Zurich, Switzerland

ABSTRACT

The assessment of the seismic performance of unreinforced masonry cross-vaults is still a challenge in numerical analysis, due to complex curved geometries and bond patterns, and uncertainties related to the selection of adequate modeling strategies, including but not limited to that of material properties, damping scheme, and unit/joint idealization. This paper presents the results of a collaborative effort to validate, against the shake table test of both unstrengthened and strengthened masonry cross-vault specimens as part of the SERA Project Blind Prediction and Post-diction Competition, various discontinuum-based numerical approaches. First, the geometry of the cross-vault is created using a Python-based computational framework to accurately represent the brick arrangement and the shape of the vault. Then, the geometry is converted into an assemblage of deformable blocks and analyzed using the Distinct Element Method (DEM). An elasto-softening contact model based on fracture energy is implemented in the masonry joints to simulate crushing, tensile, and shear failures. The performance of the proposed strategy, conceived for the unstrengthened configuration of the tested vault specimen and then adapted to include the presence of cementitious repairs, shows satisfactory agreement with both qualitative and quantitative experimental responses, also revealing critical insights and lessons learned through the blind/post-prediction exercise.

ARTICLE HISTORY
Received 7 June 2023
Accepted 20 October 2023

KEYWORDS
Blind prediction; Cross-vault; Distinct element method; Post-diction; Softening contact models; Unreinforced masonry

1. Introduction

Masonry cross-vaults are a prominent architectural feature in historic structures around the world, serving important structural roles in churches, monasteries, and monumental buildings. Formed at the intersection of two barrel vaults, masonry cross-vaults were originally developed to span wide spaces and build increasingly larger monuments (Bertolesi et al. 2019). Despite their prevalence in high seismicity areas, masonry vaults were traditionally designed to withstand only gravity loads and are therefore vulnerable to failure in seismic events. In past earthquakes, significant seismic-induced damage has been seen in masonry cross-vaults (Augenti and Parisi 2010; D'Altri et al. 2017). As many vaults function as ceilings or horizontal diaphragms, local failure can greatly influence overall structural integrity, posing a risk to human lives. The structural behavior of masonry cross-vaults is complicated by the complexities of their geometry, materials, and boundary conditions. Surveys of past earthquakes have provided information regarding the main failure mechanisms of masonry vaults, identifying the main damage patterns which can include longitudinal cracking based on abutment rocking, diagonal cracks due to in-plane shear, and delamination of ribs (Gaetani 2020). Furthermore, the vulnerability remains dependent on local geometry, material properties, loads, and construction practices. To better understand the seismic behavior, several investigations have been carried out to investigate the seismic capacity of these structures. Experimental tests have been conducted on scaled models, including quasi-static tests (Barentin, Cristián, and Block 2018; Bianchini et al. 2022; Carfagnini et al. 2018; Milani et al. 2016; Rossi, Calderini, and Lagomarsino 2016) and shake-table tests (Bianchini et al. 2022). With the limited number of full-scale tests performed on masonry cross-vaults, numerical models can add to the understanding of seismic behavior.

Modeling the dynamic behavior of masonry cross-vaults remains a challenge due to the complex

CONTACT Y.P. Oktiovan y.p.oktiovan@tudelft.nl Faculty of Civil Engineering and Geosciences, Delft University of Technology, Stevinweg 1, Delft 2628CN, Netherlands

geometrical and mechanical properties that are influenced by the original construction methods and past actions. Specifically, the inherent non-linear, anisotropic behavior of masonry (Foti, Vacca, and Facchini 2018) as well as the influence of bond pattern (Chen et al. 2021; Malomo, DeJong, and Penna 2021; Szabó et al. 2022) and interlocking add to the difficulty in creating numerical models which accurately represent the structural behavior. Numerical modeling strategies including the Finite Element Method (FEM), limit state analysis and discontinuum strategies including the Distinct Element Method (DEM) have been applied to predict the global behavior of masonry vaults. Limit state analysis relies on the upper and lower bound theorems and has been applied on vaults (Block and Lachauer 2013; Grillanda et al. 2019; Nodargi and Bisegna 2022), utilized to predict the seismic multiplier/and associated collapse mechanisms. FEM-based models can display good validation with experimental results (Carfagnini et al. 2018) and the effect of earthquakes (D'Altri et al. 2017) with macro-modeling approaches. While computational tools in FE software have greatly advanced for use in modeling complex masonry structures, including interface elements (or discontinuities) (Angjeliu, Cardani, and Coronelli 2019), there still remains room for improvement in capturing block dynamics in non-linear analyses. DEM has shown good promise for simulating the seismic response of these complex structures, as it allows for the explicit modeling of masonry's discontinuous nature.

The computational framework of DEM enables the simulation of large displacements, joint opening, and closure, as well as the complete separation of blocks from the structure (Dell'endice et al. 2021; Lemos 2007; Malomo and DeJong 2022). As such, DEM is well suited for problems concerning stability and/or collapse scenarios and has been increasingly used to analyze masonry structures (see, among others, Galvez et al. (2021); Dell'endice et al. (2022); Galvez, Dizhur, and Ingham (2023); Pulatsu, Gonen, and Lourenço (2021); Bui, Limam, and Sarhosis (2021); Meriggi et al. (2019)). Application of DEM on masonry cross-vaults has been primarily utilized in the validation of static tests, especially concerning displacements at the supports (McInerney and DeJong 2015) and the effect of ribs on vault behavior (Lengyel and Bagi 2015), while investigations into the seismic response of masonry cross-vaults are limited (Bianchini et al. 2019; Lengyel and Károly Németh 2018). Limited applications of the DEM to URM arched structures have been completed up until now, either using micro-modeling strategies (Paris, Pizzigoni, and Adriaenssens 2020; Tóth, Orbán, and Bagi 2009) or discrete meso- and macro-element modeling (Cannizzaro et al. 2018). In DEM, the mechanical interaction between the blocks that can be rigid or deformable is obtained through the point contact hypothesis, proposed by Cundall (1971). Many examples of rigid blocks are available (e.g., Foti, Vacca, and Facchini (2018) Simon and Bagi (2016)) and can be less computationally expensive in simplified micro-modeling than deformable elements. Still, the use of deformable elements can include the Poisson effect and the gyroscopic effect in dynamic evaluations (Lengyel and Károly Németh 2018).

This work presents a collaborative effort to validate a simplified DEM micro-modeling strategy for the analysis of masonry cross-vaults. The adopted modeling approach is validated against an experimental campaign of shake-table tests on a full-scale unreinforced brick masonry cross-vault conducted at *Laboratório Nacional de Engenharia Civil*(LNEC), Portugal within the scope of the SERA Project Blind Prediction and Post-Diction Competition (Bianchini et al. 2023).

The model geometry is first generated parametrically using COMPAS Masonry (Iannuzzo et al. 2021), developed using the open-source Python-based computational framework COMPAS (Van Mele et al. 2017), for the practical assessment of URM structures. The geometry is then directly translated to the DEM software 3DEC (Itasca Consulting Group Inc 2013) using *compas_3dec* (Dell'endice 2022), a package inside COMPAS Masonry for the assessment and design of unreinforced masonry structures. The generated solids are converted into an assembly of elastic blocks within 3DEC to allow elastic deformation within the blocks and the inclusion of the Poisson effect in the block units. The non-linearity is lumped at the zero-thickness interface springs formed at the contacting blocks. Elasto-softening contact models are employed to simulate crushing, tensile, and shear failures and damage in the form of crack initiation and propagation through contact and re-contact formation. The generation of the numerical models in the prediction and post-diction phases is included and compared to the experimental results to accurately inform model generation and future work.

2. Brief description of the SERA experimental campaign

This section briefly provides information pertaining to the experimental campaign carried out by Bianchini et al. (2023). In order to understand the behavior of masonry cross-vaults when subjected to seismic loads, shaking table tests were conducted on three model

configurations: a 1:5 scale cross-vault consisting of 3D-printed blocks assembled with dry joints, a full-scale model of an unreinforced masonry cross-vault, and a full-scale model of a masonry cross-vault strengthened with textile reinforced mortar. The full-scale building specimens were constructed in December 2019 and tested in LNEC in September and November 2021. For the purpose of the blind prediction and the post-diction analysis presented in this work, only the last two full-scale models are compared.

2.1. Geometrical and material properties

The detailed specification of the vault specimen is shown in Figure 1 of the Vault specimen. The full-scale model comprises a single-leaf cross-vault with a 4.4 × 4.9 m rectangular base (Figure 1a View). The vault has a rise of 1.04 m and span of 3.5 m, and comprises an orthogonal bond along the shell, with brick unit dimensions of 45 × 120 × 230 mm and a joint thickness of 10 mm along the intrados. The vault is attached to two fixed piers and two movable piers, as shown in Figure 1b.

The movable piers are steel masses with wheels that allow displacement in both horizontal directions, while the fixed piers are composed of brick units with steel stiffeners fixed to the foundation slab. All piers are connected to each another with 2xϕ32 mm steel bars to prevent rotation along the vertical axis. In order to increase the weight of the structure and further stabilize the vault, infills made out of brick units with thicker joints than the cross-vault were added to the corners of the vault.

Figure 2 setup shows the instrumentation setup used for the unstrengthened and strengthened vault specimens. The geometry of the vault shown in Figure 2 is for the unstrengthened vault, but the position and number order of the measuring instruments are exactly the same for the strengthened case. Four optical cameras (three attached to the east end of the vault and one attached to the vault crown) were used to record the displacement response at the extrados of the vault. Additionally, 17 piezoelectric accelerometers were placed surrounding the ends of the cross-vault with one additional accelerometer attached to the vault crown. The accelerometers were used to measure the modal parameters of the vault during dynamic identification tests, as well as to measure the acceleration responses during seismic tests.

To obtain the material properties of the vault, several material characterization tests were conducted. All characterization tests were done according to the respective Eurocode guidelines. In the case of the reinforced vault, the structure was strengthened via the addition of a steel and basalt grid (GeoSteel Grid 200 of Kerakoll) and lime-based mortar (GeoCalce F of Kerakoll) with 8 mm thickness to the extrados of the vault. The material properties given during the prediction stage are shown in Table 1.

Meanwhile, as the material properties of the strengthening mortar were not readily available to the authors at the prediction stage, their properties were derived from the relevant literature. The strengthening mortar material properties given at the post-diction stage are presented in Table 2.

2.2. Modal analysis and loading protocol

During the experimental loading sequence, dynamic identification tests (DITs) were conducted before each increment of the seismic load was applied. The purpose of the tests was to estimate the modal properties, e.g. natural frequencies and mode shapes,

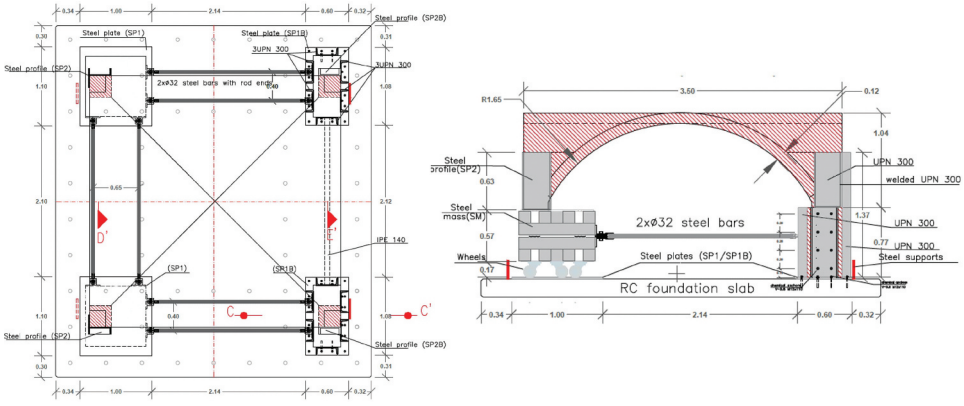

(a) Plan View (b) North view Cross Section

Figure 1. Experimental specimen detailed specifications (Bianchini et al. 2023).

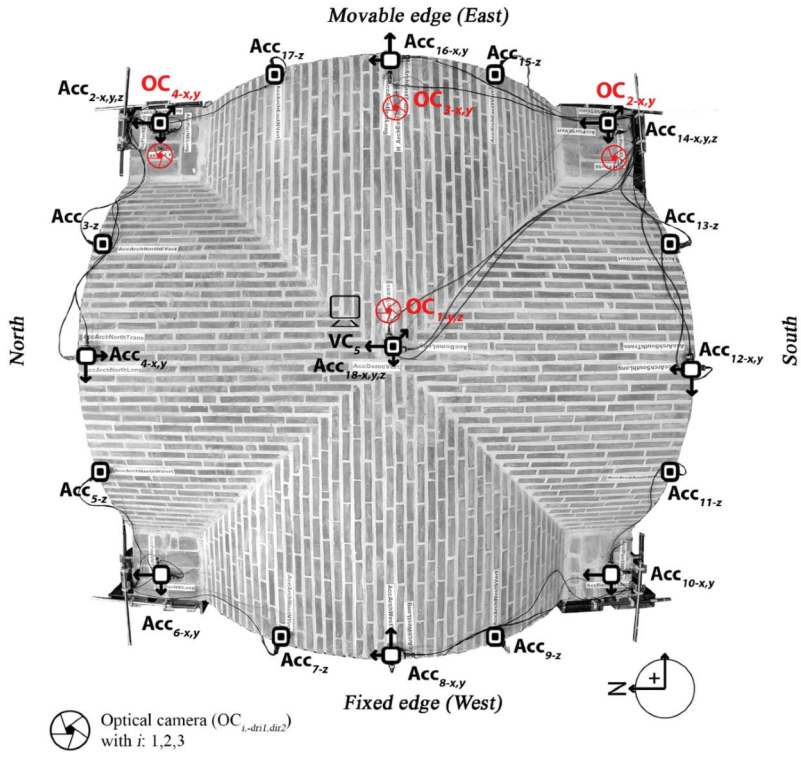

Figure 2. Instrumentation setup for the SERA cross-vault experiment (Bianchini et al. 2023).

Table 1. Selected experimental material properties considered in the numerical analysis (Bianchini et al. 2023).

Units			Mortar	Interface/joints			
Density	Young's modulus[a]	Poisson ratio	Young's modulus[a]	Tensile strength	Comp. strength	Cohesion	Friction angle
ρ	E_b	v	E_m	f_t	f_c	c	ϕ
kg/m^3	MPa	-	MPa	MPa	MPa	MPa	deg
1800	6200	0.25	370.05	0.3	9.1	0.3	38

[a]Modulus of elasticity was obtained from the average slope of the secant line at 50% and 80% compressive strength.

Table 2. Strengthening mortar material properties (Bianchini et al. 2023).

Density	Young's modulus	Poisson ratio	Flexural strength	Comp. strength
ρ	E_m	v	f_m	f_{cm}
kg/m^3	MPa	-	MPa	MPa
1870	16620	0.2	5.82	22.76

of the test specimen at both undamaged and damaged states. The DITs were conducted by applying white noise accelerations with a frequency range of 0 to 40 Hz at the shaking table base and checking the response captured by the accelerometers at the extrados of the vault.

Results from the dynamic identification tests at the undamaged states of the vault specimen, which will be shown in the post-diction analysis section, show that the first mode shape was shear in the Y-direction with a natural frequency of 6.15 Hz while the subsequent mode shapes (the second and third mode shapes) were transversal and vertical with natural frequencies of 11.62 Hz and 19.39 Hz, respectively.

The seismic load applied to the vault structures (both reinforced and unreinforced) corresponds to the seismic record of the L'Aquila earthquake that occurred on the 6th of April 2009. The seismic load was applied unidirectionally along the longitudinal

(North-South) direction of the vault specimen at 25% load increments until failure at the cross-vault was observed. For the unstrengthened case, the load was applied through the 75% seismic load increment while the strengthened case was applied until 150% of the L'Aquila EQ load input.

3. Discontinuum numerical modeling approach

3.1. Geometry generation

The experimental campaign described above is used to validate the proposed simplified micro-modeling approach. First, the model geometry is generated based on the experimental test set-up (Figure 3a) and the AutoCAD drawing provided in the blind prediction (Figure 3b). The experimental geometry is represented on a one-to-one scale, closely following the cross-vault stereotomy. Following the principles of simplified micro-modeling, the masonry units are expanded to include the 10 mm thickness of the mortar joints. This simplification is made to reduce the complexity of the model, reducing computation time (Lourenço, Rots, and Blaauwendraad 1995)

A three-dimensional representation of the cross-vault is created using COMPAS Masonry, an open-source

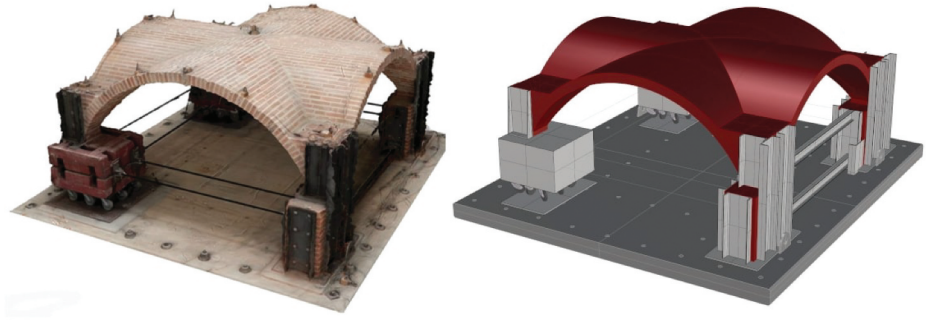

(a) Experimental Set-Up (b) AutoCAD Drawing

Figure 3. Modeled cross-vault (Bianchini et al. 2023).

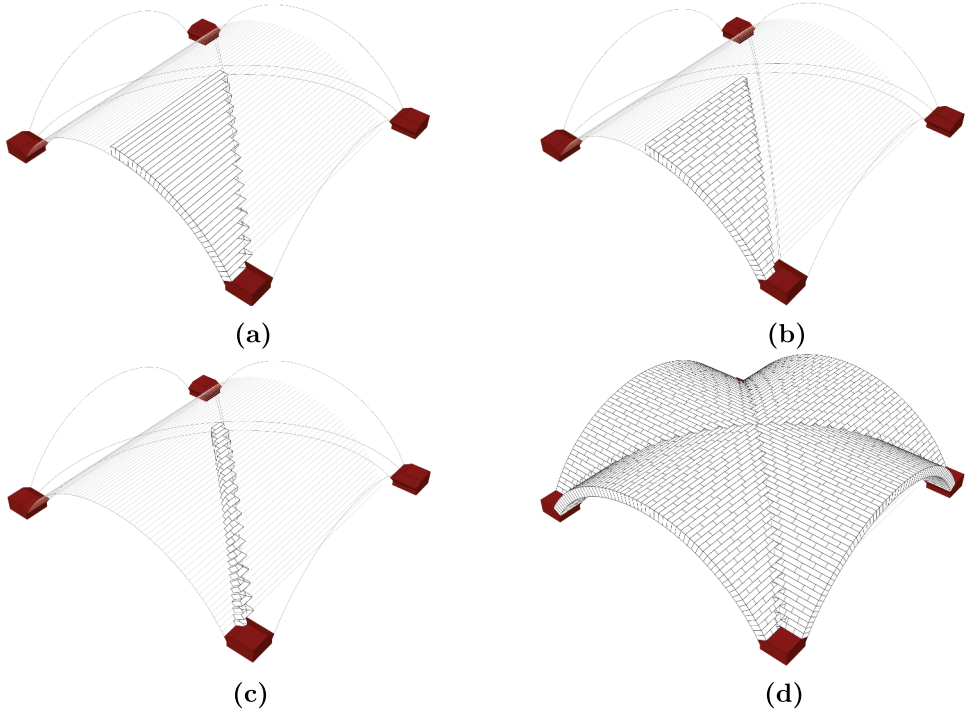

Figure 4. Parametric geometry generation a) course discretization b) fine discretization c) groin generation d) assembly of full vault.

Python-based computational framework for evaluating masonry structures (Iannuzzo et al. 2021; Van Mele 2022). Every single block in the masonry vault has been parametrically generated as a solid mesh, following the vault's stereotomy principles and replicating the discretization visible in the provided AutoCad outline of the vault. After creating the webs' blocks, the groins' blocks were generated by cutting each solid mesh multiple times, considering the intersections with the adjacent web and the staggered pattern, as shown in Figure 4.

The model is then exported from Python to the DEM software 3DEC (Itasca Consulting Group Inc 2013), using the COMPAS Masonry package for DEM, *compas_3dec* (Dell'endice 2022).

Auxillary components (e.g. steel frame, piers) are modeled as deformable blocks with relatively high stiffness values. For the strengthened case, the textile-reinforced mortar (TRM) reinforcement is represented using a thin (8 mm) layer of deformable blocks. The interaction between the vault and the reinforcement layer is controlled by the assigned joint properties, given in Table 4. The steel ties are modeled using truss structural elements with one degree of freedom at each node, perfectly connected to the piers.

3.2. Computational background- simplified micro-modeling

In DEM, masonry is modeled as a system of discrete blocks, mechanically interacting at contact points (also called sub-contacts). This discontinuum-based approach, also called simplified micro-modeling, explicitly captures the masonry texture, addressing the composite material behavior of masonry structures (Lourenço 1996). DEM relies on the numerical integration of the equations of motion to predict new block velocities and their relative displacements. Upon recognizing a contact point between discrete elastic blocks, three springs (one in normal and two in shear directions) are defined to predict the inter-block action/reaction forces (see Figure 5 Model). The present study utilizes the soft contact approach, allowing blocks to overlap based on the defined normal (k_n) and shear (k_s) contact stiffness values.

To account for deformation within the masonry units, deformable blocks are used in the model. Each deformable block is internally discretized into constant strain tetrahedral elements, with three degrees of freedom at each node (Figure 5). Note that the nodes between tetrahedral elements are referred to as gridpoints. In total, the unstrengthened and strengthened models use 1586 and 2635 deformable blocks, respectively. The varying levels of mesh refinement used in the model are shown in Figure 6 Geometry. As a result, components with coarse refinement, like the shake table and piers, have fewer gridpoints than areas with finer meshes, like the vault reinforcement. The steel ties, shown in Figure 6 Geometry, are modeled using truss structural elements with uniaxial degrees of freedom at each end node.

In DEM, the equations of motion are solved at each gridpoint using an explicit finite difference approach. Quasi-static solutions are obtained through a dynamic relaxation algorithm. First, the velocities at each node are evaluated at the mid-time step (i.e., $t^+ = t + \Delta t/2$; $t^- = t - \Delta t/2$) according to Equation (1).

$$\dot{u}_i^{t+} = \left(\left[1 - \alpha\left(\frac{\Delta t}{2}\right)\right]\dot{u}_i^{t-} + \left[\frac{\Sigma F_i^t}{m_n} + g_i\right]\Delta t\right)\left(\frac{1}{1 + \alpha\left(\frac{\Delta t}{2}\right)}\right) \tag{1}$$

where $\dot{u}$, m_n, and F are the nodal velocity vector, nodal mass, and force vector at each gridpoint. The nodal force vector, F, considers the contribution of contact forces, external forces, gravity forces, and internal stress in adjacent elements. Note that the contact forces are

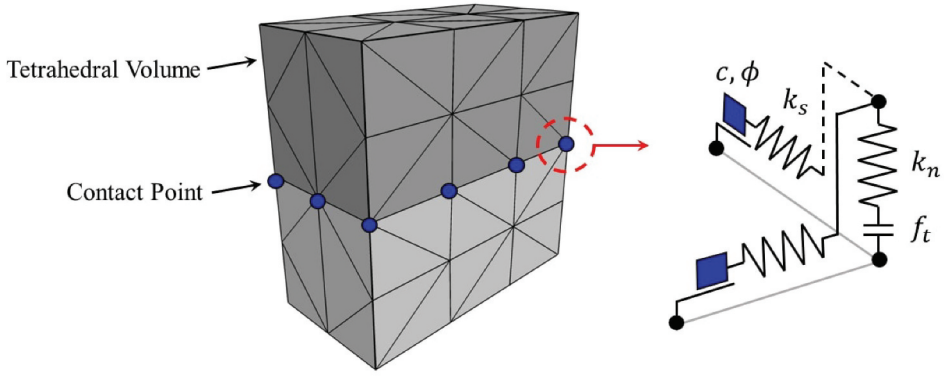

Figure 5. Representation of contact between blocks in DEM.

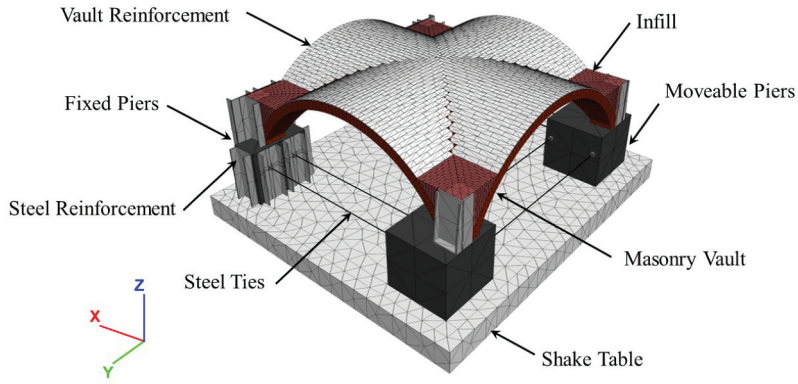

Figure 6. Model geometry in DEM.

only relevant for gridpoints located along the contact surface. Internal nodal forces F_k^{int}, are obtained using Equation (2).

$$F_k^{int} = \int_s \sigma_{kj} n_j ds \tag{2}$$

where n_j is the unit normal to the surface S and σ_{kj} is the tetrahedral element stress tensor. In 3DEC, quasi-static solutions are obtained by dynamic relaxation. For quasi-static solutions, an adaptive global damping scheme is adopted in the present research, in which the viscous damping constant (α) is adjusted throughout the simulation to ensure that the ratio between the damping power and the rate of change of kinetic energy in the system remains constant (e.g. 0.5) (Cundall 1982; Hart, Cundall, and Lemos 1988). Mass-proportional Rayleigh damping is employed in the dynamic analyses, allowing results to be obtained in a reasonable time frame.

Once the position of each block is updated by integrating the nodal velocities, the relative displacements between adjacent blocks are found in the normal (Δu_n) and shear (Δu_s) directions at each sub-contact. It should be noted that throughout the dynamic solution procedure, contact points are updated using the common-plane hypothesis, as described by Cundall (1988). The corresponding elastic stress increments in the normal ($\Delta\sigma$) and shear directions ($\Delta\tau$) are calculated at each contact point according to Equation (3). New contact stresses are found by adding the calculated elastic increment to the stress from the previous timestep, shown in Equation (4).

$$\Delta\sigma = k_n \Delta u_n; \Delta\tau_{s,i} = k_s \Delta u_{s,i} \tag{3}$$

$$\sigma^{t+} = \Delta\sigma + \sigma^t; \tau_{s,i}^{t+} = \Delta\tau_{s,i} + \tau_{s,i}^t \tag{4}$$

If applicable, the updated contact stresses are corrected according to the defined failure criteria. The current study utilizes linear elastic deformable blocks, therefore consolidating all non-linearity at the contact points. To best represent the experimental results, different contact constitutive models are adopted between different model components. In the following sections, three main stress-displacement laws are employed: the elastic joint model, the Mohr–Coulomb joint model, and the bilinear fracture energy-based elasto-softening contact model described in Pulatsu et al. (2019), Pulatsu et al. (2020), and Pulatsu et al. (2020). These three joint contact models are illustrated in Figure 7.

In the elastic joint model, the contact behavior is controlled by the normal and shear stiffness parameters with no yield criteria. The Mohr–Coulomb joint model introduces a cut-off in tension (f_t) and shear (τ_{max}; based on normal stress (σ), cohesion (c), and friction angle (ϕ)). A residual shear capacity (τ_{res}) is defined in terms of the normal stress, residual cohesion (c_{res}), and residual friction angle (ϕ_{res}).

The fracture energy-based elasto-softening contact model offers a bilinear softening response for tension, shear, and compression, including the mode-I (G_f^I), mode-II (G_f^{II}), and compressive (G_c) fracture energies, respectively. The fracture energies used are calculated according to Equations (5) to (7) (Lourenço 2010).

$$G_c = 15 + 0.43 f_c - 0.0036 {f_c}^2 \tag{5}$$

$$G_f^I = 0.025 (2 f_t)^{0.7} \tag{6}$$

$$G_f^{II} = 10 G_f^I \tag{7}$$

Finally, the numerical stability of the computational procedure is dependent on the time-step. A critical time-step (Δt_c) is automatically calculated according to Equation (8) (Lemos 2008), based on the nodal stiffness (k_{gp}) and nodal mass (m_n). Note that the nodal stiffness considers both the stiffness of the tetrahedral element (k_{tet}) and,

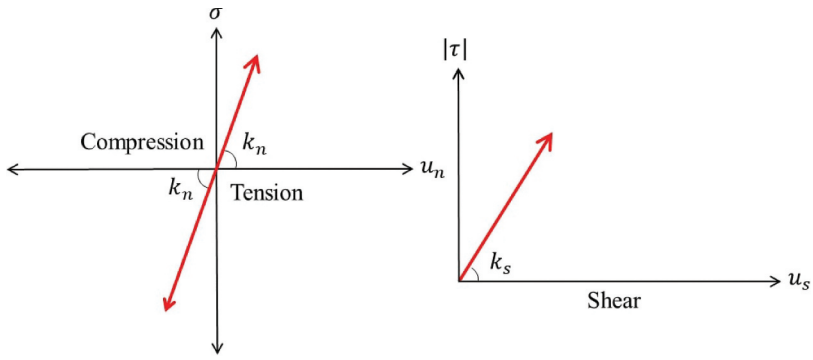

(a) Elastic joint model

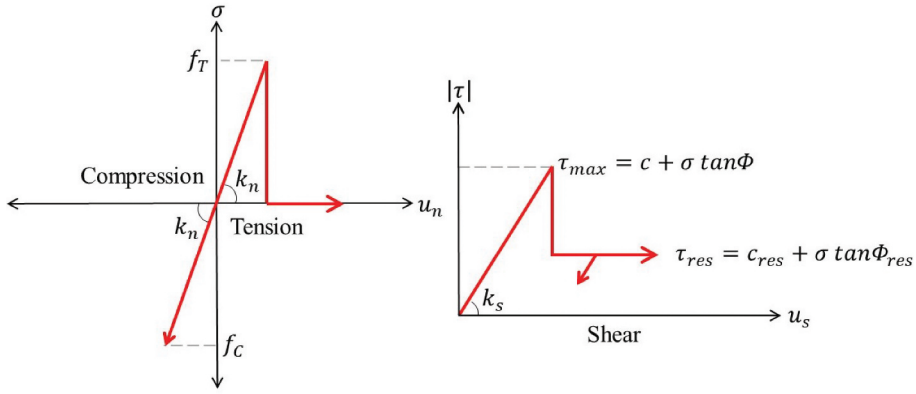

(b) Mohr-Coulomb joint model

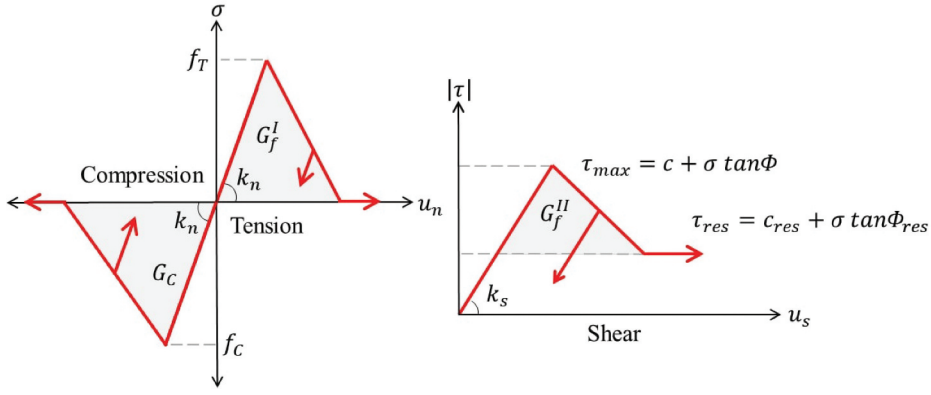

(c) Fracture energy-based elasto-softening joint model

Figure 7. Adopted contact constitutive models.

where applicable, the stiffness of the contact (k_n). The equation for the stiffness of the tetrahedral element is given in Equation (9), where K, G, A, and h are the bulk modulus, shear modulus, area of the tetrahedral, and minimum height of the tetrahedron, respectively.

$$\Delta t_c = 2\sqrt{m_n/k_{gp}} \tag{8}$$

$$k_{gp} = k_n + k_{tet}; k_{tet} = \left(K + \frac{4}{3}G\right)\left(\frac{3A}{h}\right) \tag{9}$$

3.3. Loading and boundary conditions

Using the simplified micro-modeling approach described above, the cross-vault is first brought to equilibrium under gravity. The gravitational acceleration is applied to the model in 10 steps, with each increment corresponding to 0.98 m/s^2. The model is brought to equilibrium after each increment. Nonlinear dynamic analyses are then conducted to simulate the experimental shake table test. The provided ground motion is input into 3DEC as a velocity time history. To reduce the computation time, the input

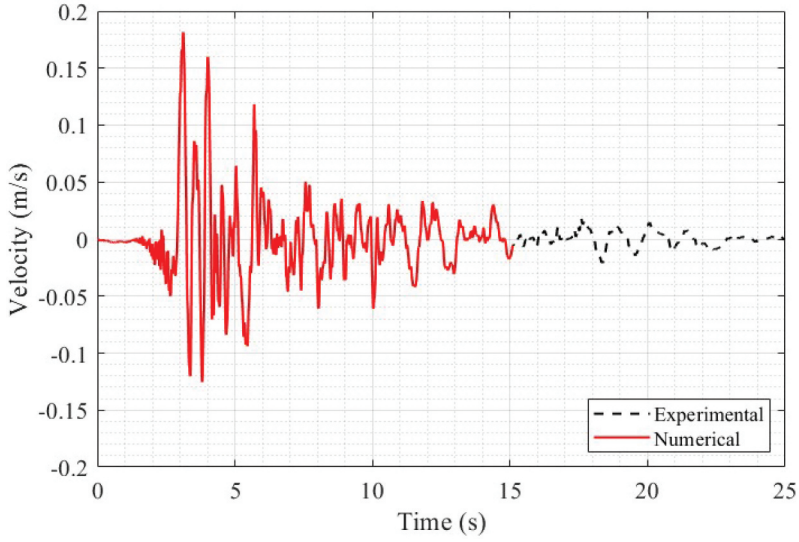

Figure 8. Experimental and truncated numerical velocity time history (L'aquila 75%).

ground motion is shortened to the initial 15 s, as this period is the most destructive (Figure 8). The time-varying velocity boundary is applied directly to the shake table in the global Y direction (refer to Figure 6). Movement in the shake table is restricted in the global X and Z directions, rotation is also prevented. The rolling piers (shown in black in Figure 6) are simulated by allowing them to move in the X and Y direction, rotation about the Z axis is also permitted. Conversely, the movement of the fixed piers (shown in white in Figure 6) is restricted in all directions.

The displacement of the vault is monitored at the locations shown in Figure 9. At the monitoring locations, the acceleration is calculated from the model displacement using a MATLAB ODE solver. The average acceleration is obtained by approximating the velocity in a given time increment. In the following discussion, the model displacements will be compared to those recorded by the experiment's optical cameras. Similarly, the calculated accelerations will be compared to those recorded by the accelerometers. Qualitative comparisons will be made on the observed damage and crack patterns.

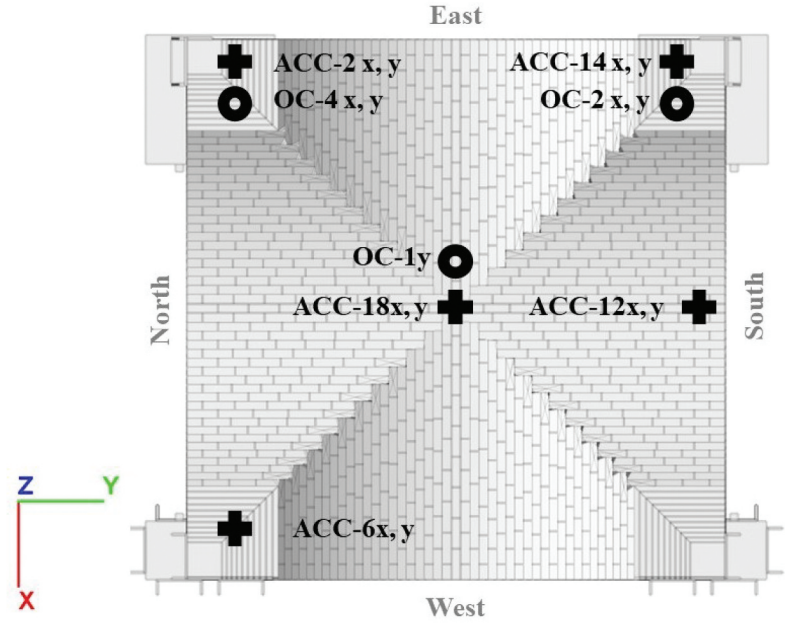

Figure 9. Accelerometer (ACC) and optical camera (OC) placement.

4. Blind prediction analysis

4.1. Model parameters

The blind prediction analyses were conducted in 3DEC 5.2 (Itasca Consulting Group Inc 2013). After the model geometry has been imported into 3DEC the blocks are discretized into linear elastic tetrahedral volumes. A total of 32,667 tetrahedral elements and 23,819 nodes are present in the unstrengthened model. In the strengthened model, this total increases to 52,791 tetrahedral elements and 41,575 nodes.

As described in Section 3.2, three different joint constitutive models are adopted. To best capture the experimental results, the fracture energy-based elasto-softening joint model is defined throughout the vault, infills, and vault reinforcement (see Figure 10). The elastic joint model is defined for sub-contacts between the steel components and the rest of the model. Finally, the Mohr–Coulomb slip model is used to simulate a dry joint connection between the moveable piers and the shake table.

The parameters used to define the models are derived from the provided material characterization test results (Bianchini et al. 2022). Different material properties are assigned to different components in the model (see Figure 11).

These properties have been summarized in Table 3. Furthermore, the properties defined between blocks, including the properties within the reinforcement elements, are provided in Table 4.

4.2. Unstrengthened case results

The comparison between numerical analysis at the blind prediction stage and the experimental results was made in terms of natural frequency from the modal analysis, crack patterns at the end of load application, displacements at the extrados of the vault, and acceleration responses from the accelerometers.

4.2.1. Qualitative response comparisons

First, the result from modal analysis from experiments and numerical analysis are compared. Because 3DEC 5.2 does not allow eigenvalue analysis for deformable blocks, the Fast Fourier Transform was applied, using SeismoSignal Seismosoft (2002), to the displacement time history recorded in free vibration at the crown of the cross-vault. This free-vibration state was calculated by applying a linearly increasing acceleration at the shake table along the seismic load direction and which was then abruptly stopped. The vault was then left to free-vibrate after this initial stage. Figure 12 shows the first mode shape obtained from the numerical modal analysis at the undamaged state of the cross-vault. At the blind prediction stage, the numerical model was only able to reproduce the first mode shape from the experiment. The first mode natural frequency observed

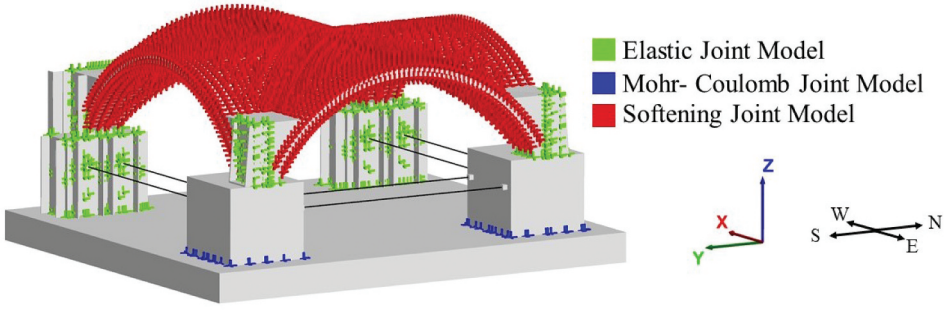

Figure 10. Definition of joint constitutive relations.

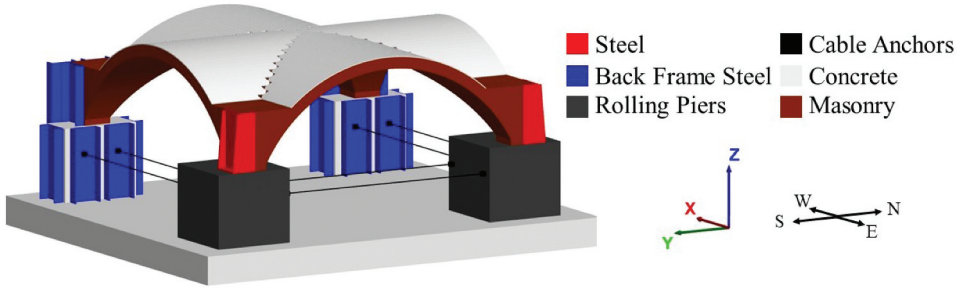

Figure 11. Material properties within the model.

Table 3. Material properties used in the numerical analysis.

Component	Density ρ kg/m^3	Young's modulus[a] E GPa	Poisson ratio v -
Steel	7780	200	0.3
Back Frame Steel	10685	200	0.3
Rolling Piers	5570	200	0.3
Cable Anchors	2000	200	0.3
Concrete	2000	25	0.3
Masonry	1800	6.2	0.25

[a]Modulus of elasticity was obtained from the average slope of the secant line at 50% and 80% compressive strength.

from the experiment was 6.15 Hz compared to 12.5 Hz obtained from the numerical analysis. However, the mode shape of the experimental results was simulated relatively well with shearing movement along the Y-direction observed at the movable piers.

With respect to the crack pattern at the end of load application, a generally good agreement was observed between the experimental and numerical results, as illustrated by Figure 13. The crack pattern of the numerical model was obtained by plotting the coupled shear-tensile damage parameter based on the formulation of Pulatsu et al. (2020). No damage was found at the seismic load increment of 25% and 50%.

The numerical model was able to simulate the cracks along the four vault diagonals as well as the cracks close to the fixed piers. However, the model was unable to simulate the longitudinal cracks at the vault webbing (along the X-direction), and the large transversal crack at the vault between the fixed piers (along the Y-direction). This could partially be attributed to existing light damage within the vault, amplified by the sequential seismic load increments applied to the vault specimen.

4.2.2. Quantitative response comparisons

Aside from qualitative comparison, the numerical model is also quantitatively validated against the

Table 4. Joint properties used in the numerical analysis.

Joint Model		Normal stiffness k_n GPa/m	Shear stiffness k_s GPa/m	Tensile strength f_t MPa	Comp. strength f_c MPa	Cohesion c MPa	Friction angle ϕ deg
General	Elastic	100	100	-	-	-	-
	Mohr- Coulomb	10	10	0	-	0	5
	Fracture Energy- Based	8.744	3.498	0.3	9.1	0.3	38
Reinforcement	Within Reinforcement	5000	2000	100	1000	100	45
	Between Reinforcement and Vault	2500	1000	50	50	50	45

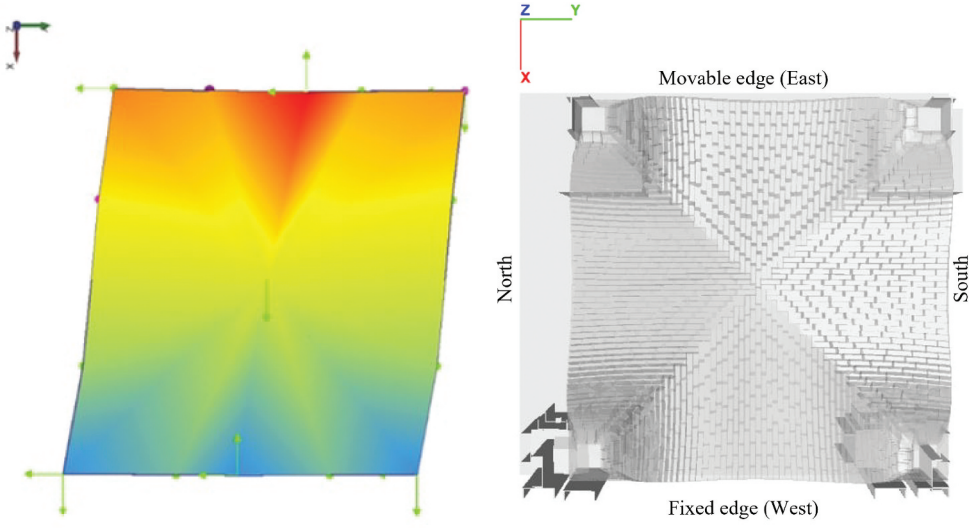

(a) Experimental (b) Numerical

Figure 12. First mode shape comparison between experimental and numerical analysis at prediction stage.

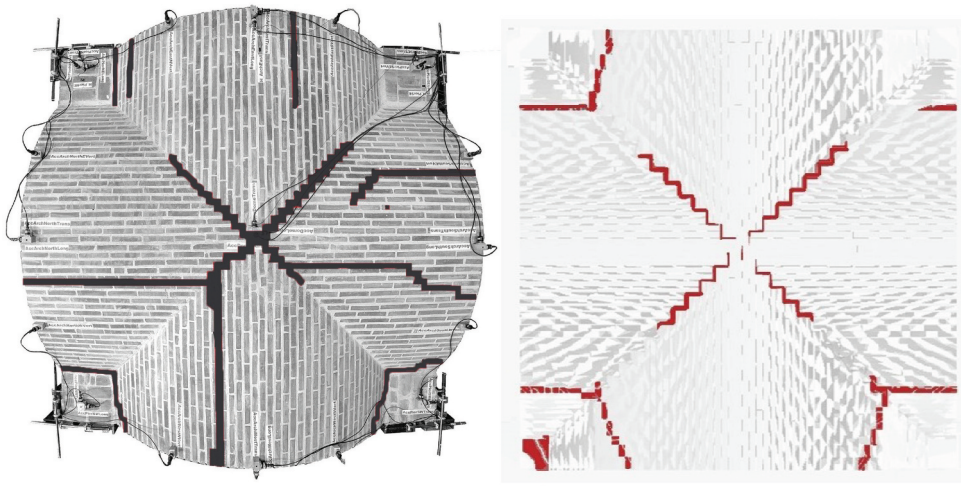

(a) Experimental (b) Numerical

Figure 13. Comparison of (a) experimental (Bianchini et al. 2023) and (b) numerical crack patterns at the vault extrados.

experimental results in terms of recorded displacements and acceleration responses. It is important to note that in the experiment, the optical cameras registered residual displacements after dynamic identification tests before the seismic load was applied at 50% and 75% load increments. Thus, to facilitate comparison with the numerical results, the experimental displacement responses were initialized by subtracting all values from the initial displacements.

A comparison of the absolute maximum total displacements recorded from the optical cameras and the corresponding location in the numerical model is shown in Table 5. The numerical model generally underestimated the observed displacements at the vault with errors ranging from 16% to 46% in the longitudinal (Y) direction (the direction in which the input signal was applied), to 70% in the transversal (X) direction. A full comparison of displacement vs time history at each measurement point is shown in Figure 14. Relatively good agreement between the two sets of results was observed particularly at the displacement responses along the Y-direction. Slight differences between the two results could be partly attributed to the "perfect" conditions of the numerical model which assumes that the blocks are perfectly connected without any pre-existing damage, which is seldom the case in experiments or reality.

On the other hand, the displacement responses along the transversal direction were not well captured by the numerical model. This could be attributed to the nonlinearity that was not captured in the numerical model, e.g. the longitudinal cracks at the vault webbing that induced additional displacements when the joints were opening. This will be addressed further in the postdiction analysis of the unstrengthened vault case.

With regards to the total accelerations, the numerical model was found to overestimate the response of the

Table 5. Absolute maximum total displacements (mm) and accelerations (m/s^2) comparisons between experiment and numerical analysis of unstrengthened case.

		Experimental	Numerical	Relative Error (%)
Displacement (mm)	OC1-y	32.0	27.2	−15.6
	OC2-x	4.4	1.3	−70.5
	OC2-y	52.5	28.4	−45.9
	OC4-x	7.8	2.2	−71.8
	OC4-y	32.1	27.6	−14.0
Acceleration (m/s^2)	ACC2-x	4.4	7.2	−63.6
	ACC2-y	4.5	4.6	−2.2
	ACC6-x	4.0	1.4	65.0
	ACC6-y	4.5	3.3	−26.7
	ACC12-x	3.4	3.7	−8.8
	ACC12-y	4.9	4.3	12.2
	ACC14-x	5.2	3.0	42.3
	ACC14-y	4.4	3.7	15.9
	ACC18-x	3.8	4.6	−21.1
	ACC18-y	3.4	4.4	−29.4

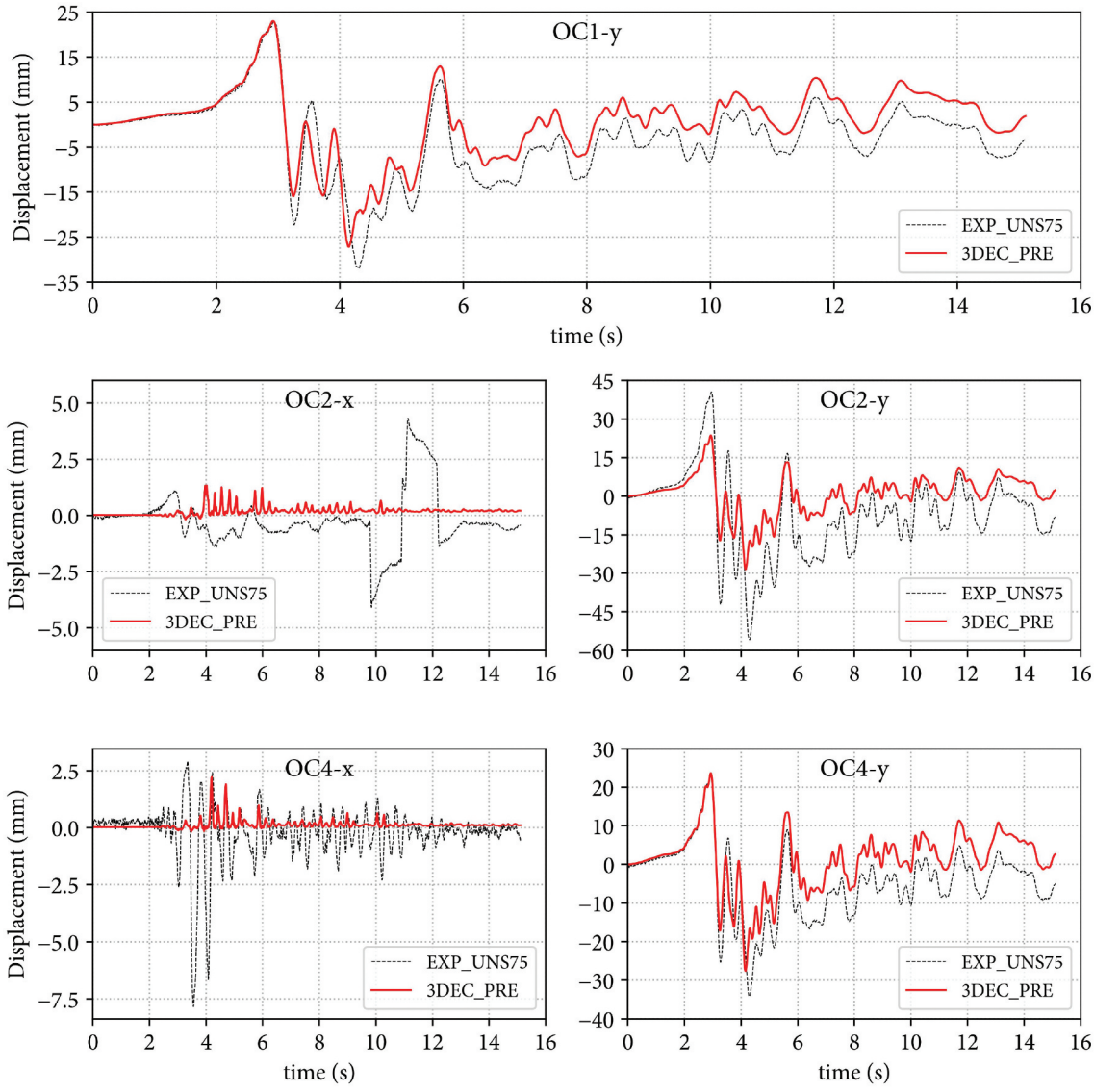

Figure 14. Experimental and numerical comparison of displacement responses at each optical camera at 75% load increment (unstrengthened case).

experimental specimens at all monitored accelerometers, as shown in Table 5, with relative errors ranging from 2.2% to 65%.

The full comparison of acceleration time history is presented in Figure 15. Even though the amplitude comparison was in good agreement between experimental and numerical results, the numerical model was unable to capture the transient high amplitude between $t = 2.0$ to $t = 3.0$ s at every measurement point. The overestimated response was most likely caused by the use of mass-proportional damping in the numerical model (see Hall (2006)). For non-linear models where progressive softening can occur, the system's response during softening is controlled by the deformation modes at frequencies lower than the natural frequency. Therefore, the damping due to the mass-proportional part increases significantly, resulting in an overestimated capacity of the structures, as discussed by Lemos and Sarhosis (2023). While the use of either stiffness-proportional or Rayleigh damping would have solved this issue, they demand a smaller time step compared with only mass-proportional damping, where the time step due to the stiffness-proportional component reduces by one or two orders of magnitude. For a complex and large model such as this cross-vault model, the computational effort increases exponentially.

The overestimated response could also be attributed to the higher stiffness of the numerical model, which then correlated to the higher natural frequency (12.5 Hz) compared to the experimental system (6.15 Hz at the undamaged state, which decreased to 5.89 Hz as

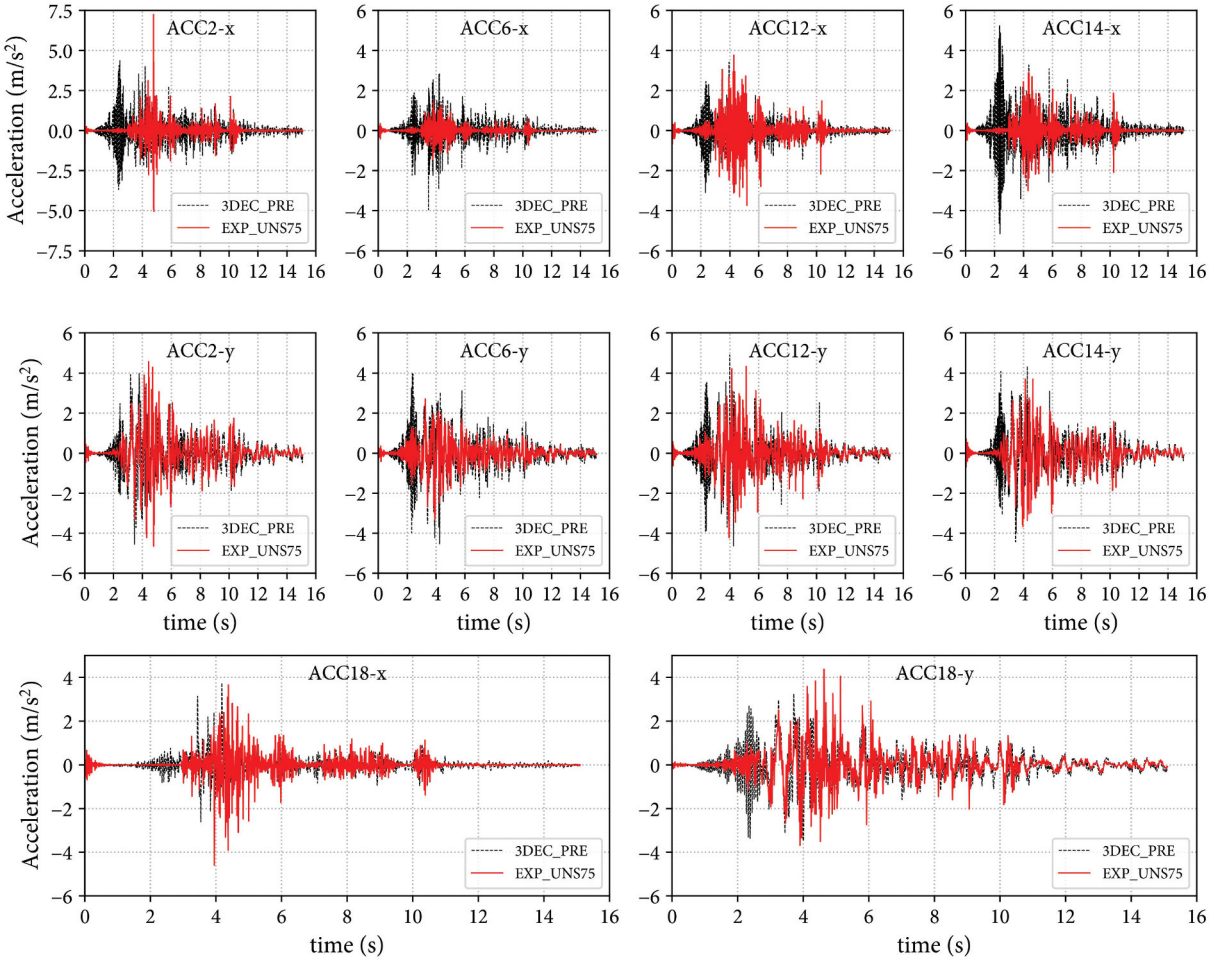

Figure 15. Comparison of acceleration responses at selected accelerometers at 75% load increment (unstrengthened case).

damage accumulated during the seismic tests). For the post-diction analysis, the stiffness of the numerical model was calibrated to match the experimental results. Regardless of these discrepancies, the numerical model is still able to reproduce the displacement and acceleration responses relatively well, both quantitatively and qualitatively.

4.3. Strengthened case

4.3.1. Qualitative response comparisons

The comparison between numerical analysis and the experiment in the prediction case follows a similar approach for the strengthened case. In the strengthened model, the same vault properties and geometry were utilized as in the un-strengthened case, serving as a baseline. An additional 1 cm layer of reinforcement was incorporated, modeled as a discontinuous assembly of linear elastic solid elements (E_{TRM} = 50000 MPa). The cross-section of the reinforcement elements matched that of the bricks, enabling displacement and damage mapping of the reinforcement. This choice was made as continuous curved elements encountered convergence issues in 3DEC. The strengthened model underwent analysis using a similar non-linear dynamic process, considering cumulative damage at 100%, 125%, 150%, 175%, and 200% of the applied earthquake signal. Signals prior to 100% were excluded from the cumulative analysis due to minimal observed damage up to 75%, with noticeable damage initiating only at 100%. The first 15 s of each signal was applied, as in the unstrengthened model shown in Figure 8. Focusing solely on the final stages of applied loads improved analysis efficiency by reducing computational power and time requirements. Furthermore, a truncated portion of the earthquake signal, spanning from 2.9 to 5.9 s, was considered. This period encapsulated the highest input within the seismic signal. To expedite the numerical analysis, only this condensed segment of the signal was taken into account. Due to time limitations, the same modal analysis performed on the unstrengthened model was not replicated in the pre-test simulation. Nevertheless, the incorporation of reinforcement allowed for a reasonable assumption of increased model stiffness.

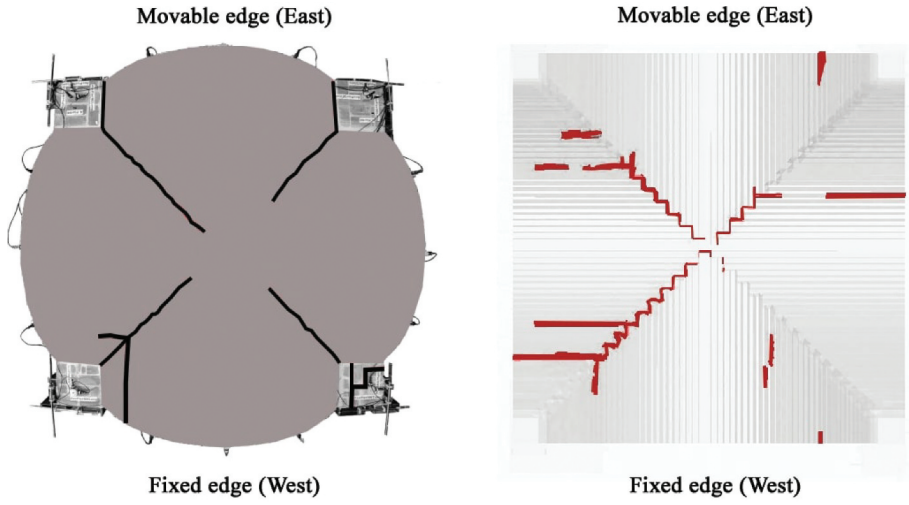

(a) Experimental (b) Numerical

Figure 16. Comparison of strengthened crack patterns at the vault extrados.

The failure of the strengthened vault comprised shear failure through the formation of cracks along three of the vault diagonals (NE, SE, NW) while hinges were also observed to develop along the eastern and western edges of the vault. Rocking mechanisms, in opposite directions, resulted from the hinge formation. Additionally, minor cracking could be observed at the northern and southern edges, along horizontal joints. Most of the damage occurred in the intrados, with very limited damage observed in the reinforcement itself, as shown in Figure 16. In comparison to the experimental results, the same failure mechanism and cracking along the diagonals were observed. The numerical model was able to simulate well the rocking mechanism and detachment of the supports, yet was unable to simulate the severe cracking close to the supports.

4.3.2. Quantitative response comparisons

Recorded displacement and acceleration results measured at the 150% case of the applied earthquake load can be validated quantitatively against the experimental behavior. As in the unstrengthened case, a comparison of the absolute maximum total displacements recorded from the optical cameras was conducted using the initialized experimental data. A comparison of the recorded displacements at each of the optical cameras is included in Table 6.

As Table 6 indicates, the numerical model recorded significantly lower displacements than its experimental counterpart. The differences in displacement measurements (ranging from 77% to 98%) could be attributed to the higher stiffness of the model and/or the shortened signal periods applied to the model. Considering that a lower level of damage was observed in the numerical analysis than

Table 6. Absolute maximum total displacements and acceleration comparison between experiment and numerical analysis of strengthened case.

		Experimental	Numerical	Relative Error (%)
Displacement (mm)	OC1-y	57.21	1.12	−90.75
	OC2-x	39.68	0.59	−98.73
	OC2-y	64.02	2.34	−92.34
	OC4-x	14.38	0.80	−77.28
	OC4-y	62.63	2.26	−82.17
Acceleration (m/s^2)	ACC2-x	10.02	9.3	−7.19
	ACC2-y	9.41	14.7	56.22
	ACC6-x	11.73	8.8	−24.98
	ACC6-y	9.04	9.2	1.77
	ACC12-x	9.46	11.3	19.45
	ACC12-y	8.35	43.2	417.37
	ACC14-x	17.32	12.3	−28.98
	ACC14-y	10.50	64.7	516.19
	ACC18-x	8.17	4.2	−48.59
	ACC18-y	7.65	10.1	32.03

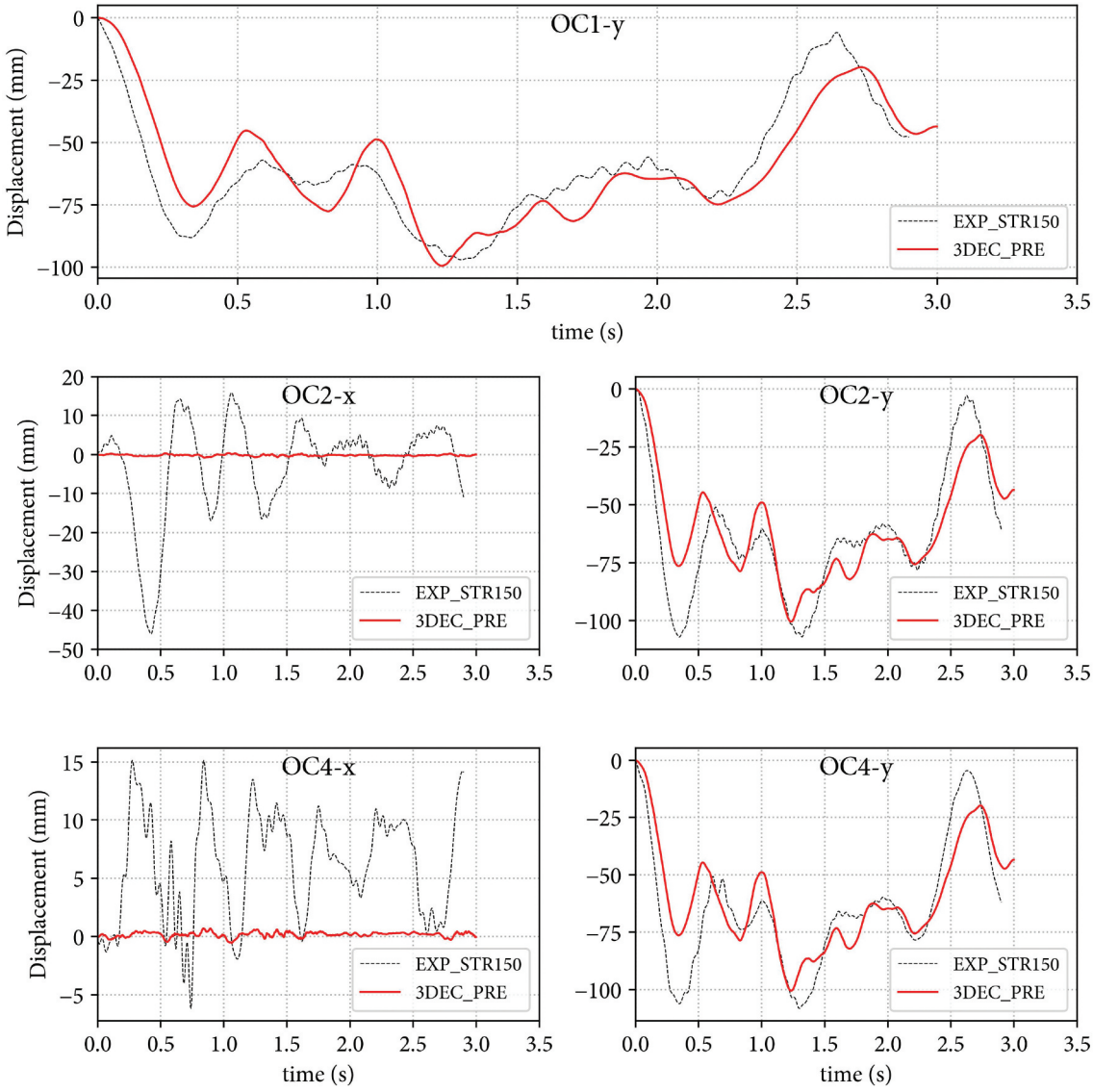

Figure 17. Comparison of displacement responses at each optical camera at 150% load increment (strengthened case).

in the experiment, smaller displacements show a correlation to greater model stiffness. Additionally, larger displacements in the experiment could be attributed to the damage accumulation from the previous tests. While displacements in the X-direction are severely underestimated in the numerical analysis, a much better correlation is observed in the Y-direction (Figure 17).

With respect to the total acceleration response, the results of the experiment and numerical model were predicted overall quite well, as observed in Table 6. The relative error in the X-direction ranged from 7.2% to 48.6%, while in the Y-direction from 1.8% to 517%. The overestimation of the acceleration response in the Y-direction could be attributed to the higher stiffness of the model than the experimental case, as considered in the unstrengthened case. The use of mass-proportional damping at 6% in the numerical model can also contribute to the overestimation of the response. However, the response of the system overall followed closely with the experiment (Figure 18).

While the results from the blind prediction analysis demonstrate that the numerical model had a higher stiffness than the experiment in addition to an overestimation of accelerations and underestimation of displacement, it was however able to produce the same failure mechanism and a majority of the damage. The post-test calibration to the experiment of material properties, damping, and the meshing scheme can aid in reducing the errors to provide a better-detailed response replicating the experiment.

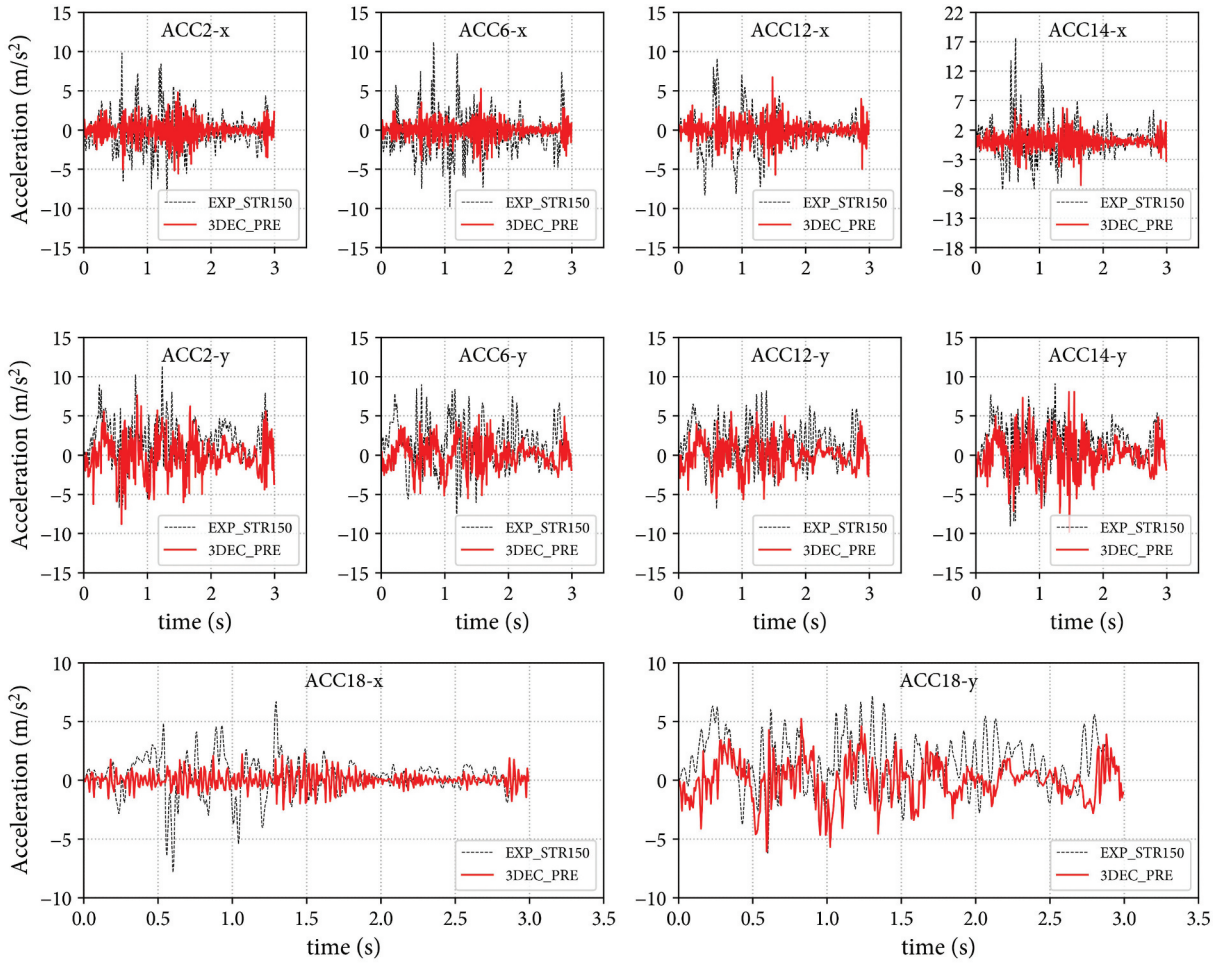

Figure 18. Comparison of acceleration responses at selected accelerometers at 150% load increment (strengthened case).

5. Post-diction analysis

5.1. Calibration of modeling parameters

5.1.1. Calibration of modeling techniques

The post-diction analyses are performed in 3DEC 7.0 (Itasca Consulting Group Inc 2013), allowing eigenvalue analyses to be undertaken for deformable blocks. This capability is not available in 3DEC 5.2, meaning that any eigenvalue analyses must be performed during post-processing. The direct eigenvalue analysis capability in 3DEC 7.0 simplifies the calibration process in the post-diction numerical model. To improve the model's efficiency, the meshes in the post-diction are improved from those used in the blind prediction. To improve the model's efficiency, the meshes in the post-diction are improved from those used in the blind prediction. While the mesh refinement does not have a significant impact on the numerical results, the elimination of small, irregular, and distorted elements (see Figure 19) helped to reduce the computation time. The changes in block discretization and internal meshes are summarized in Table 7, where the number of nodes, tetrahedral volumes, and degrees of freedom is given for all of the models. From the blind prediction, the number of elements has been reduced by 34.2% in the unstrengthened case and 48.6% in the strengthened model.

5.1.2. Calibration of material parameters

To better represent the experimental results, the joint parameters from the blind prediction are adjusted for the post-diction. The first change made is to the contact properties between the shake table and the rolling piers. The material table function is utilized to reduce the normal and shear stiffness for newly generated sub-contacts by 50%. In the strengthened case, the contact stiffness is adjusted to better capture the response of the cross-vault. The normal and shear joint stiffness values are reduced by 75% both within the reinforcement and at the respective contact points.

While the authors acknowledge that the numerical model of masonry structures are often sensitive to the

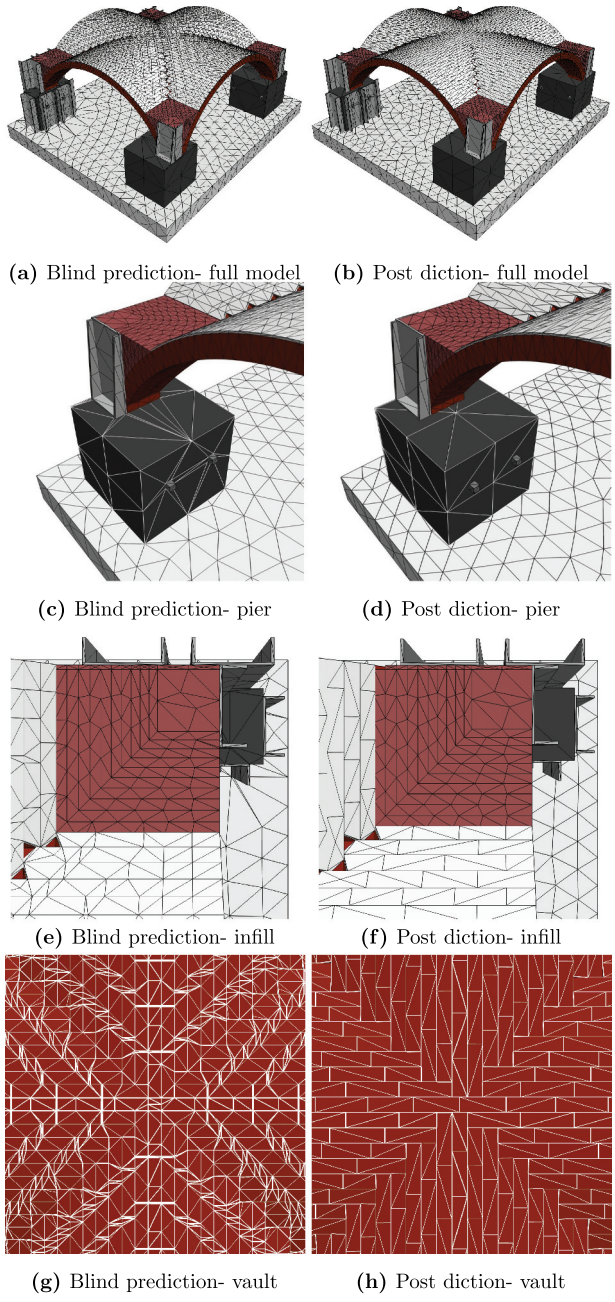

Figure 19. Mesh refinement.

change of fracture energy (see Pulatsu (2023), Bejarano-Urrego et al. (2018), and Pluijm van der (1997)), this research opts for the practical utilization of an empirically derived fracture energy equation (Equation (5) to (7)) without further calibration of the parameter. The decision to employ this equation stems from the time-intensive nature of calibrating the fracture energy within the cross-vault model. Nevertheless, this paper seeks to streamline the modeling process while maintaining a credible representation of fracture behavior in masonry structures.

5.1.3. Calibration of damping ratios

In the blind prediction, the damping ratio tested (6%) was found to be too high. Therefore, to investigate the effect of the damping ratio on the dynamic response of the vault, two different damping ratios were tested on both the unstrengthened and strengthened models (3% and 4%). The max displacement results for the two ratios are plotted against experimental results in Figure 20. In the unstrengthened case, the 3% damping ratio showed a slight improvement over the 4% damping ratio. However, since the acceleration and crack pattern of the 4% damping ratio model matched better to the experimental results, 4% damping is used for the unstrengthened case instead. Conversely, in the strengthened case, the 4% damping ratio more closely simulated the experimental testing, particularly in the y-direction.

5.2. Unstrengthened case results

Similar to the comparison of experimental results at the prediction stage, the natural frequency from the modal analysis, crack patterns at the end of load application, displacements at the extrados of the vault, and acceleration responses from the accelerometers were compared between the experimental and numerical results.

5.2.1. Qualitative response comparisons

The modal analysis at the post-diction stage was conducted differently compared to the blind prediction modal analysis. Instead of applying Fast Fourier Transform and leaving the vault to free-vibrate, the

Table 7. Comparison of mesh refinement.

	Unstrengthened			Strengthened		
	Blind prediction	Post-diction	% Change	Blind prediction	Post-diction	% Change
nodes	23819	17295	−27.4	41575	25552	−62.7
tetrahedral volumes	32667	21489	−34.2	52791	27158	−48.6
degrees of freedom	148263	93564	−36.9	239397	145020	−39.4

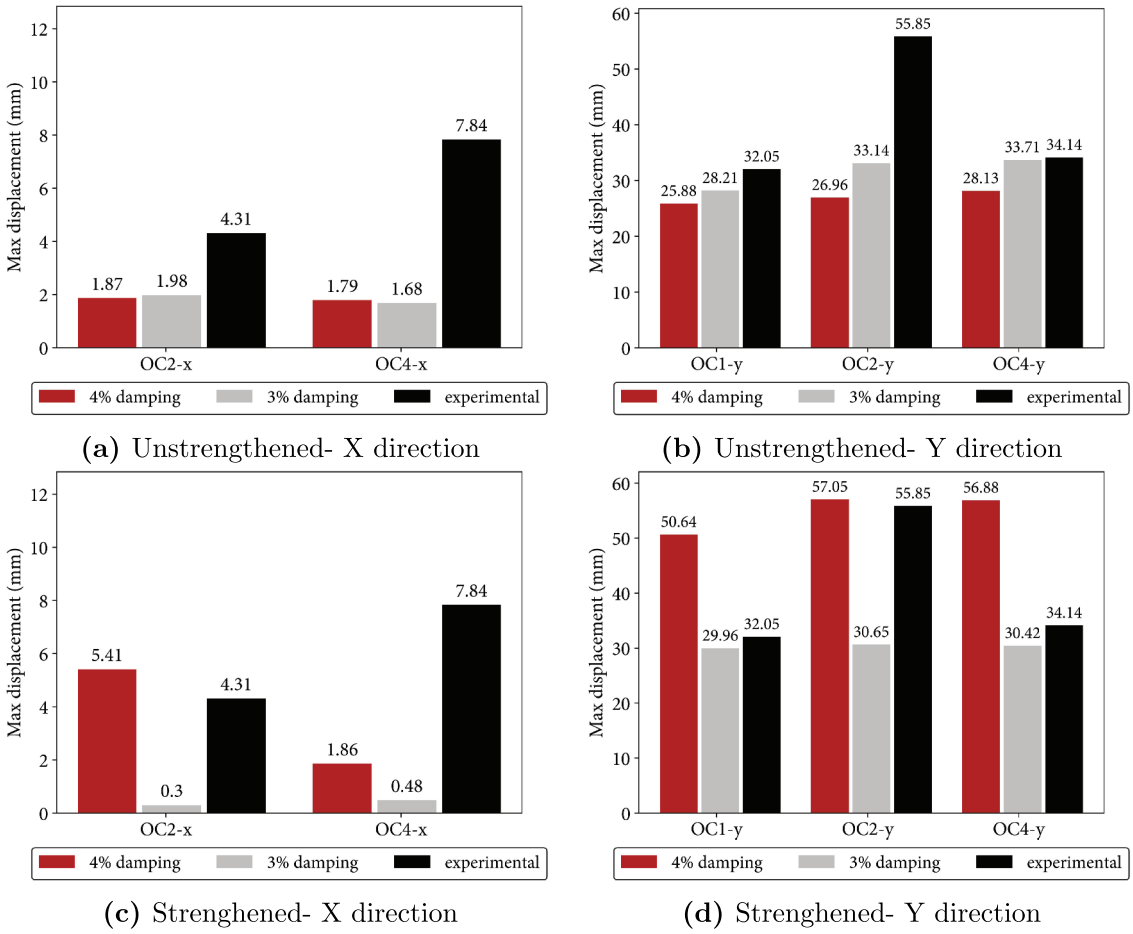

Figure 20. Damping calibration.

Table 8. Modal analysis comparison of experimental and numerical — UNS case.

Mode	Mode Shape	Experimental Hz	Numerical Hz	Relative Error %
1	Shear	6.15	6.66	8.29
2	Transverse	11.62	6.79	41.57
3	Vertical	19.39	21.54	11.09

simple power iteration method is used to calculate the eigenvalue of the vault system. Under a specific mode shape, the algorithm will iterate to find the dominant eigenvalue given an arbitrary starting vector. With this method, the numerical mode shapes other than the first mode can also be compared against the experimental results.

Table 8 presents the eigenvalue analysis result from the experimentally measured responses and numerical analysis of the cross-vault at the undamaged state. It can be observed that the numerically predicted natural frequency for the first and third modes matches relatively well with the experimental results while the second mode was underestimated.

The comparison of experimental and post-diction numerical mode shapes is shown in Figure 21. The first and second modes from the experimental result correspond to the actual first and second modes of the numerical model while the third mode from the experimental results corresponds to the seventh mode of the model since the ordering is not exact. The contours shown in both figures are normalized displacement magnitude with red color indicating maximum displacement magnitude while blue color indicates zero displacement magnitude. The undeformed shape of the vault is presented in Figure 21d to 21f in blue shade. It can be seen that the numerical model managed to simulate the first mode relatively well where the movable

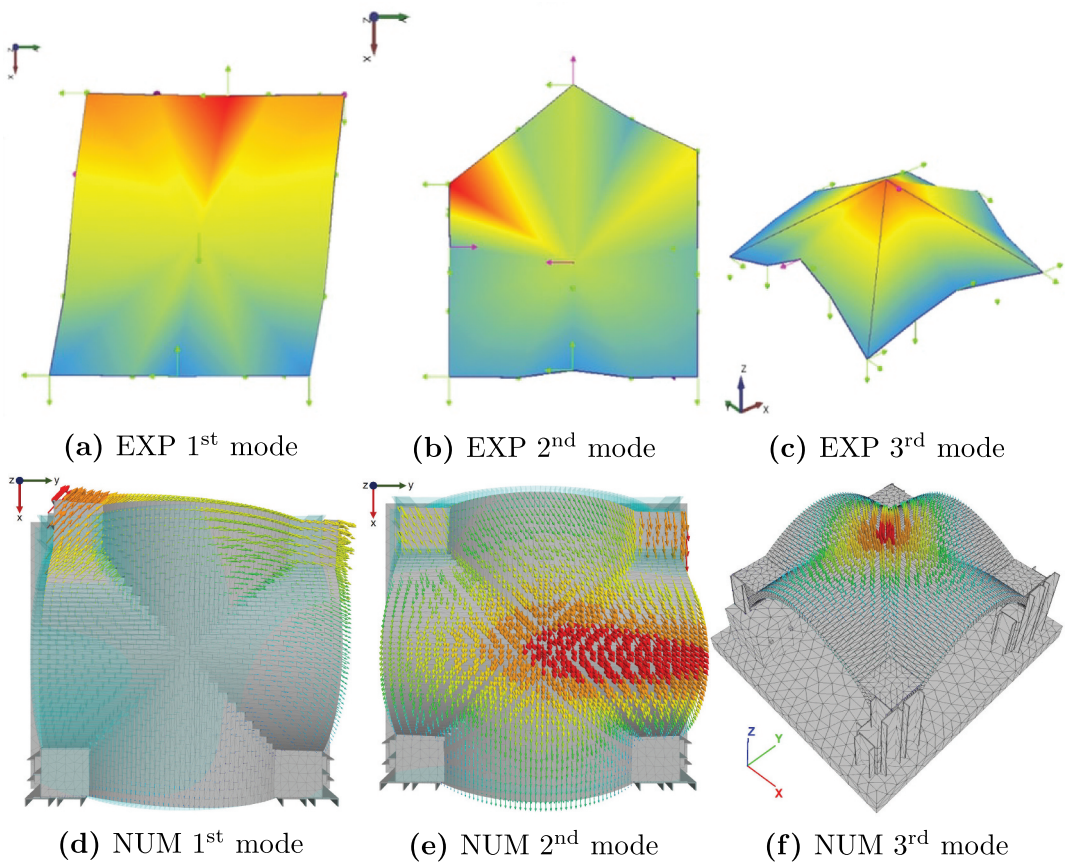

Figure 21. Comparison of mode shapes.

piers deformed along the Y (North-South) direction. However, while the maximum displacement occurred at the vault between the movable piers in the experimental result, the maximum displacement for the first mode shape of the numerical model occurred at the South movable pier. This difference could be caused by the fact that the numerical model took into account the displacement at the intrados of the arch as well as the lateral section of the vault while the experimentally recorded values were taken only at the extrados of the arch.

For the second mode, where the mode shape was orthogonal to the first mode, the numerically predicted response was relatively different than the experimental mode shape. In the experimental second mode, the maximum displacement was localized towards the South movable pier, resulting in an asymmetric movement between the movable piers. Meanwhile, the numerical second mode was symmetric with equal movement on both piers. Finally, the third numerical mode shape was in good agreement with the experimental counterpart, where the maximum displacement occurred at the crown of the cross-vault.

Aside from the comparison of eigenfrequencies and visual comparison of the mode shapes, the Modal Assurance Criterion (MAC) between each relevant mode shape is also compared as an additional confidence factor for the evaluation of modal vectors at measured locations (see Pastor, Binda, and Harčarik (2012)). The MAC comparison is conducted to check whether the mode shapes from experimental results and those from the numerical analysis are highly correlated or not. The MAC value is calculated using Equation (10) below for a n number of measured points:

$$MAC(A,X) = \frac{|\sum_{j=1}^{n} \phi_{A_j} \phi_{X_j}|}{\sum_{j=1}^{n} \phi_{A_j}^2 \sum_{j=1}^{n} \phi_{X_j}^2} \tag{10}$$

where ϕ_{A_j} and ϕ_{X_j} are the experimental and numerical modal vectors at measurement point j, respectively. It is important to note that the MAC values are indications of consistencies, not validities, hence the compared values should not indicate whether the compared numerical mode shapes are valid or not, but whether the compared mode shapes are highly correlated or not.

The MAC values comparison between experimental and numerical mode shapes for the unstrengthened case is presented in Figure 22. While the MAC percentages at the diagonal (comparison of relevant mode shapes between 3DEC and EXP) are relatively high, the

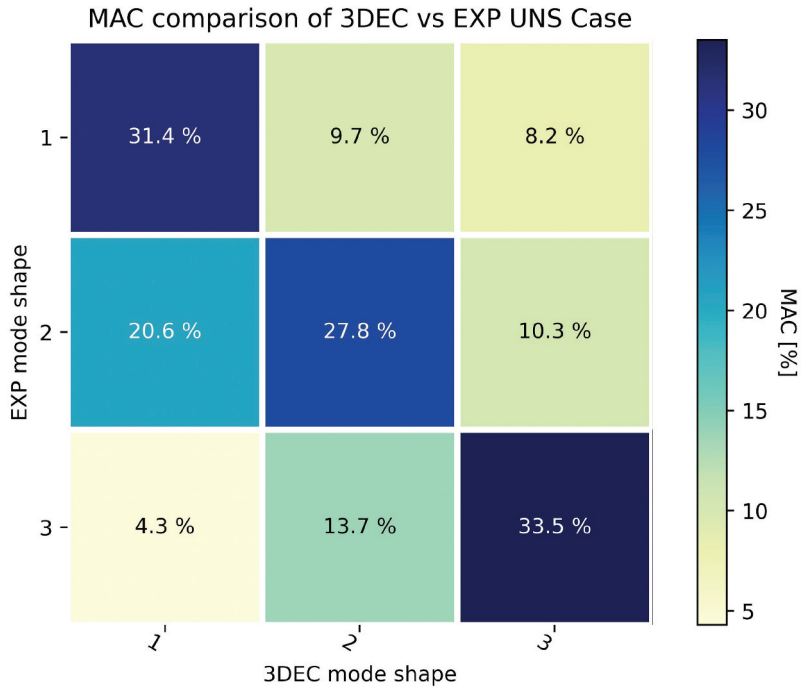

Figure 22. MAC Comparison of 3DEC and EXP for the UNS-POST case.

percentage is still well below 50%. Improvements with regard to the modal analysis for the numerical model will be considered as the future work of this paper.

The damage pattern of the unstrengthened cross-vault model at the end of each load increment is shown in Figure 23. As a comparison, the crack pattern at the end of each load increment for the blind prediction, and the experimental result are presented as well. It is important to note that similar to the blind prediction stage, only the first 15 s of the ground motion input signal is applied to the model, as this was observed to be the most destructive. The input signal was applied for 15 s on one load increment and then scaled up to the next load increment for the next phase of the dynamic analysis.

The vault was still pristine at 25% load increment on both the numerical model and experimental specimen. Damage occurred from the 50% load increment, approximately at the 3 to 4 s of the seismic load excitation. As shown in Figure 23b, the damage occurred from the crown of the vault and propagated towards all directions of the groins. This was not the case for the blind prediction model (Figure 23a), where only separation between the infill elements and the vault at the South-east corner had occurred. With regards to the experimental crack pattern (Figure 23c), it has been informed that the cracks did originate from the crown of the vault. However, the cracks closed at the end of the seismic load application due to self-weight. The experimental footage was taken at the very end of the seismic load application ($t = 25.0$s in Figure 8).

Finally, Figure 23e can directly be compared to Figure 23f. The failure of the unstrengthened cross-vault was observed at the 75% load increment, where debonding of the bed joints within the cross-vault web-bing was observed, in contrast to the crack pattern of the blind prediction at the 75% load increment (Figure 23d). It is clear that when debonding occurred on one side of the vault, it also occurred on the orthogonal vault, forming an L-shaped damage pattern. Damage also occurred at the connections between the cross-vault and the infill elements, similar to the experimental crack pattern in Figure 23f. However, the damage at the connections between the cross-vault and the infill elements occurred at all corners of the vault while it only happened at the fixed edge of the vault for the experimental crack pattern.

5.2.2. *Direct vs incremental dynamic analysis*

In order to highlight the effect of incremental dynamic analysis, the vault model was subjected to a dynamic load with intensity directly equal to 75% of the L'Aquila EQ, instead of applying the dynamic load incrementally from 25% to 75%. The displacement responses and crack pattern are shown in Figures 24 and 25 respectively.

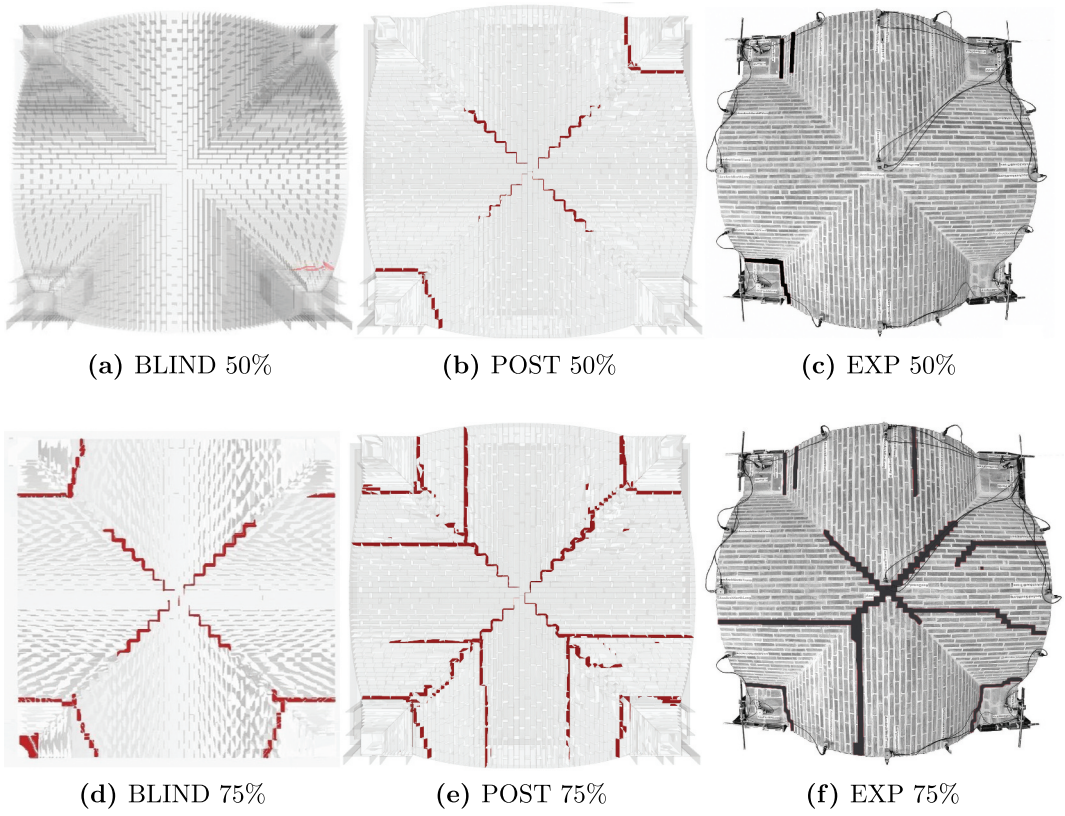

Figure 23. Comparison of crack patterns of the unstrengthened vault between blind prediction, post-diction, and experiment at selected load increments.

While the displacement response at the crown of the cross-vault (OC1-y in Figure 24) showed no significant differences between direct and incremental seismic load, the responses on the other optical cameras were generally different. On both OC2-y and OC4-y, the direct seismic load model underestimated the negative peak displacement observed in the experiment at approximately 3.0 s to 4.0 s.

The crack pattern comparison of both dynamic loading scenarios is shown in Figure 25. The similarity found in OC1-y (Figure 24) could be attributed to the fact that the damage on both models originated from the crown of the vault, and then propagated to the groins. In contrast to the incremental dynamic analysis model, the direct seismic model experienced light damage across the bed joints in all directions as well as concentrated full damage along the groin side of the cross-vault. Meanwhile, the incremental dynamic analysis model experienced localized damage towards the cross-vault, the bed joints within the masonry webbing, and the pier-vault connections.

5.2.3. Quantitative response comparisons

For the quantitative comparison, the evolution of the displacement response at each load increment is presented in Figure 26 to highlight the effect of the incremental dynamic analysis to the displacement response. At the 25% load increment (Figure 26a), the numerical model was in a good agreement with the experimentally observed results even at the later time step of the dynamic analysis where the numerical response started to slightly deviate from the experiments from 10 to 15 s. As the load increment increased to 50% (Figure 26b), the deviation at the later time step became apparent but the numerical peak displacement response from 3 to 4 s was still in a good agreement with the experimental result. Finally, the differences between the numerical and experimental responses became more obvious at the 75% load increment (Figure 26c).

Similar to the prediction model, this discrepancy could be caused by non-linearity and imperfect conditions of the experimental specimen that were not captured in the numerical model. In general, the insight about numerical models often disregarding the 'imperfections' from experimental research is essential, as it underlines the gap between theoretical and real-world complexities. Integrating experimental data into the numerical model could enhance its accuracy and reliability, further aiding in the understanding of the actual behavior of the tested structures.

The absolute maximum displacements of the post-diction numerical model are also provided in Table 9.

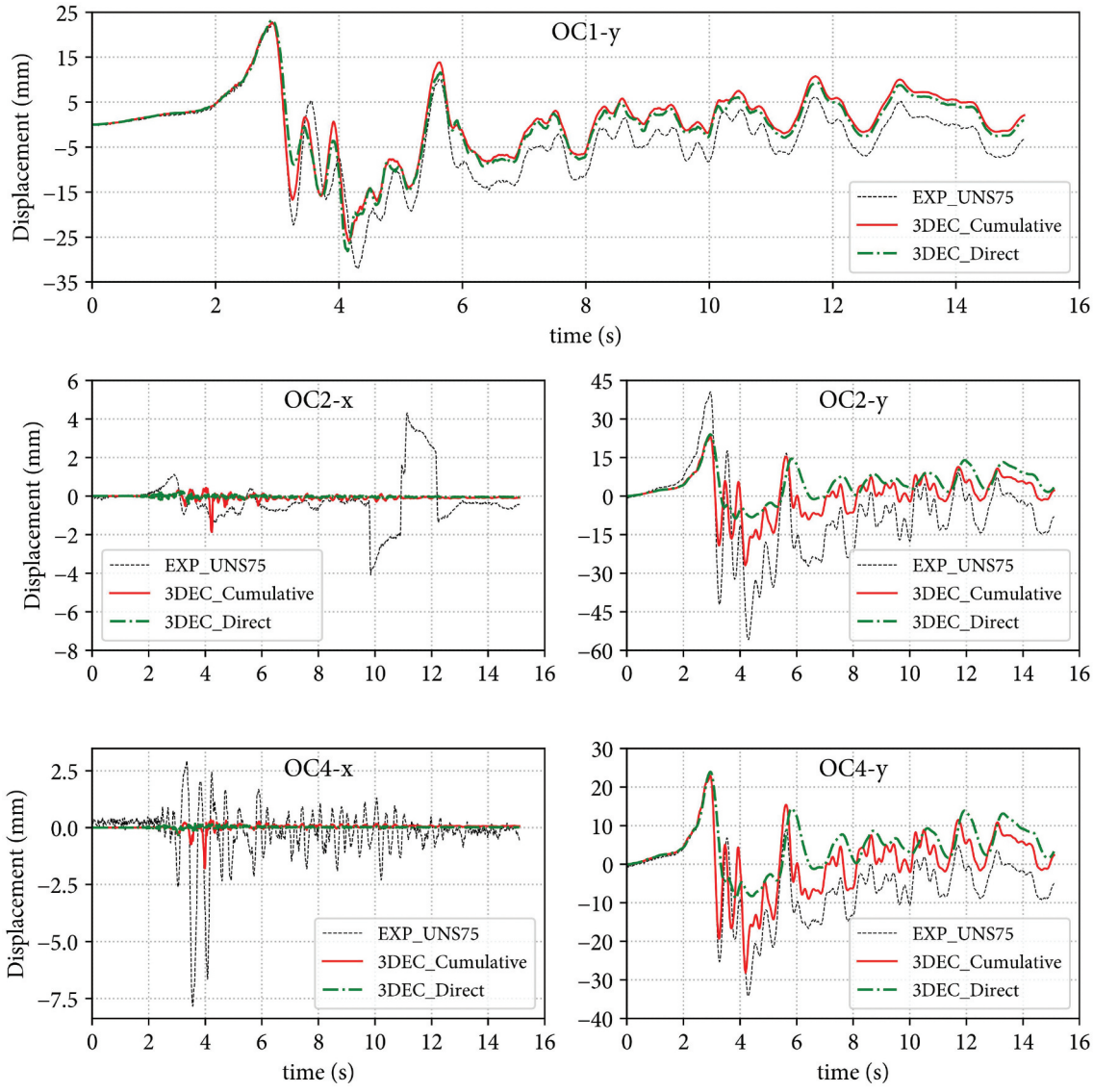

Figure 24. Comparison of displacement responses between direct and incremental.

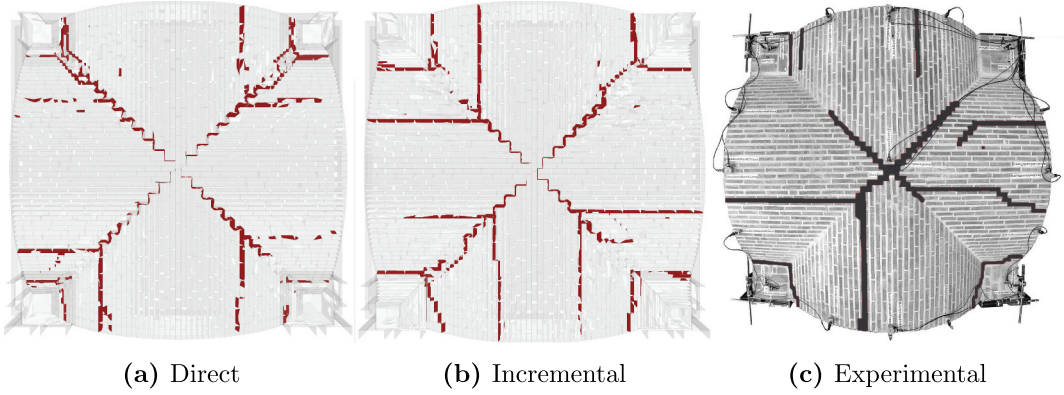

(a) Direct (b) Incremental (c) Experimental

Figure 25. Comparison of crack pattern between direct and incremental seismic load.

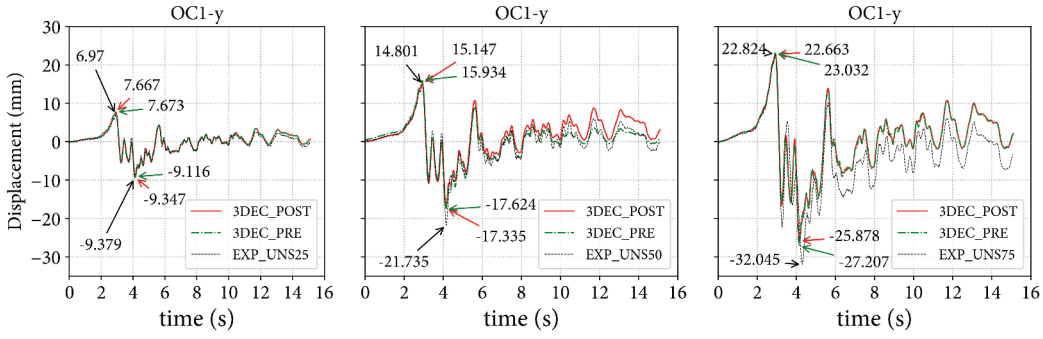

(a) 25 % OC1-y (b) 50 % OC1-y (c) 75 % OC1-y

Figure 26. Comparison of displacement evolution at OC1-y.

Table 9. Absolute maximum total displacements and acceleration comparison between experiment and post-diction numerical analysis of unstrengthened case.

			Post-diction		Pre-diction	
		Experimental	Numerical	Relative Error (%)	Numerical	Relative Error (%)
Displacement (mm)	OC1-y	32.0	25.8	−20.2	27.2	−15.6
	OC2-x	4.4	1.8	−59.1	1.3	−70.5
	OC2-y	52.5	26.9	−48.8	28.4	−45.9
	OC4-x	7.8	1.8	−76.9	2.2	−71.8
	OC4-y	32.1	28.1	−12.5	27.6	−14.0
Acceleration (m/s^2)	ACC2-x	4.4	5.1	−16.6	7.2	−63.6
	ACC2-y	4.5	6.1	−35.3	4.6	−2.2
	ACC6-x	4.0	1.7	57.5	1.4	65.0
	ACC6-y	4.5	1.5	66.7	3.3	−26.7
	ACC12-x	3.4	3.8	−11.8	3.7	−8.8
	ACC12-y	4.9	2.6	46.9	4.3	12.2
	ACC14-x	5.2	2.8	46.2	3.0	42.3
	ACC14-y	4.4	4.1	6.8	3.7	15.9
	ACC18-x	3.8	3.2	15.8	4.6	−21.1
	ACC18-y	3.4	2.6	22.3	4.4	−29.4

Similar to the prediction stage, the numerical model still underestimated the observed displacements with errors ranging from 12% to 49% in the longitudinal direction and close to 80% for the transversal direction. The displacement responses observed at each optical camera on the 75% load increment are shown in Figure 27. The difference between the prediction and post-diction numerical result for the displacement along the longitudinal direction is relatively small, as the model already had a good agreement in that direction. However, the displacement response along the transversal direction was noticeably higher on the post-diction model. This could partly be attributed to the calibration of material parameters and better definition of contacts between each element of the cross-vault. Based on the experimentally observed values, it is evident that there was an asymmetric movement at the transversal direction, where OC4-x recorded a peak displacement almost twice as much as the South side counterpart OC2-x. This, however, was not captured by the numerical model as the orthogonal to the seismic direction movement was symmetric.

The total acceleration responses observed at the post-diction model for the 75% seismic load increment are also presented in Table 9. There are no noticeable differences in terms of the acceleration responses along the X and Y direction of the experimental results, which is the same case for the numerical model. The relative errors now ranged from 7% to 67%, with most responses from the post-diction model underestimating the acceleration response from the experimental results. The full acceleration responses at selected accelerometers are shown in Figure 28.

Similar to the blind prediction model, the numerical model was still unable to capture the high amplitude response between $t = 2.0$ to $t = 3.0$ s, as the post-diction model still used mass-proportional damping, only with lower base frequency (12.5 Hz for the prediction model compared to 6.66 Hz for the post-diction model). As part of the future work of this paper, a different damping scenario

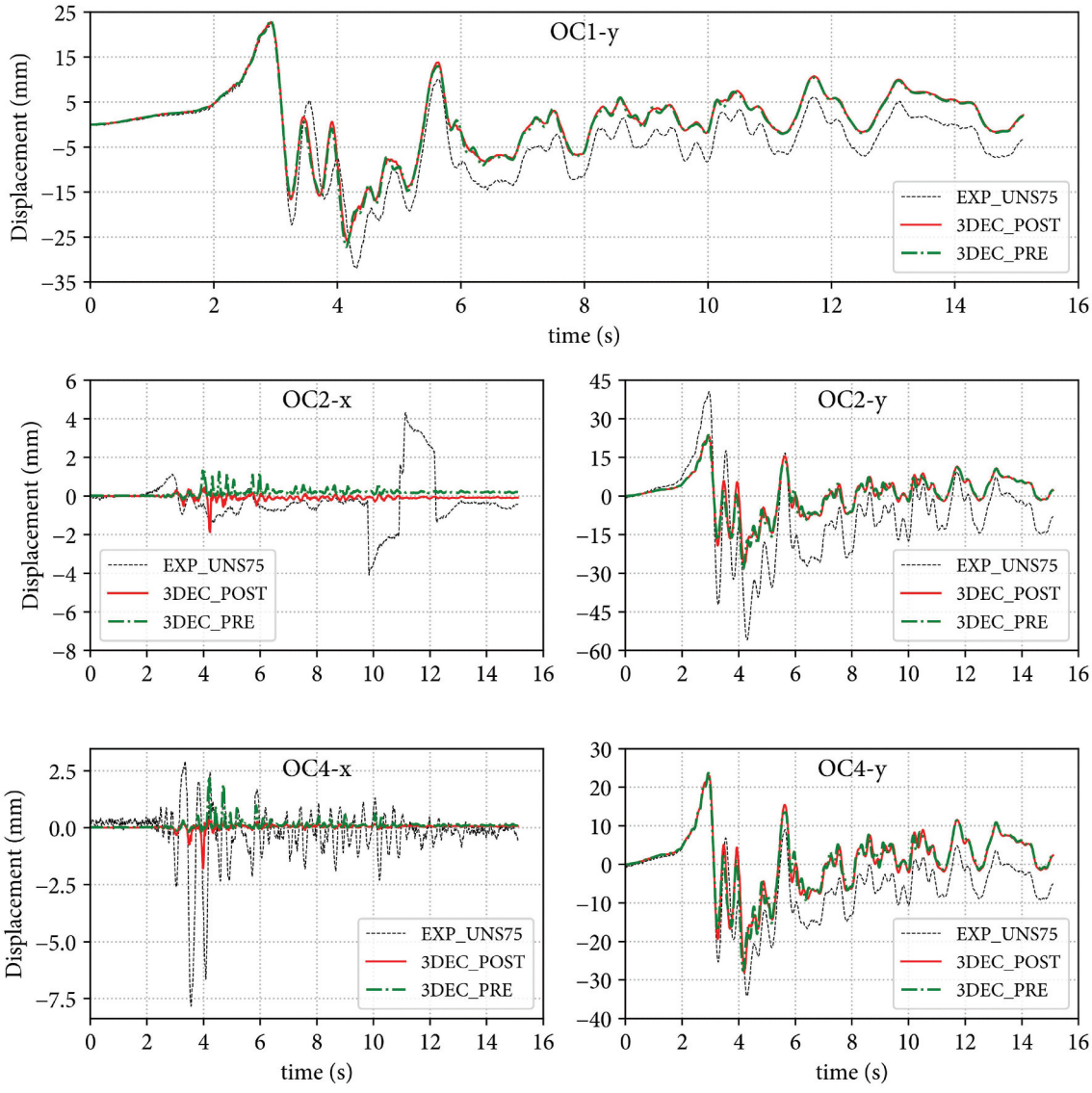

Figure 27. Comparison of displacement responses at each optical cameras on the 75% load increment (unstrengthened case).

will be considered, specifically via the use of Maxwell elements at discrete joints that respond to the relative displacements and velocities (Lemos and Sarhosis 2023).

5.3. Strengthened case results

5.3.1. Qualitative response comparisons

The calibration of the post-diction numerical model of the strengthened case was conducted using an eigenvalue analysis, similar to the unstrengthened case. The natural frequency of the model and the first 10-mode shapes were calculated using the power iteration method. For the strengthened case, only two mode shapes were calculated during the experimental phase and the comparison between the first two modes is shown in Figure 29. In this figure, the contour vectors in red correspond to the maximum displacement and blue to the minimum displacement. The undeformed vault is displayed in blue to show the deformation of each mode. The first mode, for both the numerical and experimental models, displays a shear mode shape with the greatest displacement at the base of the movable piers in the Y-direction (North-South). The frequency of the numerical model (7.59 Hz) displays a slightly stiffer setup than the experimental test (6.15 Hz) with a 23% relative error, yet this discrepancy can be attributed to the increased stiffness of the reinforcement. The frequency of the first mode of the experiment in the unstrengthened vault was also 6.15 Hz. The calibration of the strengthened model was completed considering just the first mode shape as the second mode of the experiment corresponds best to the second eigenmode of the numerical model. In the post-test phase, the cumulative dynamic analysis was completed

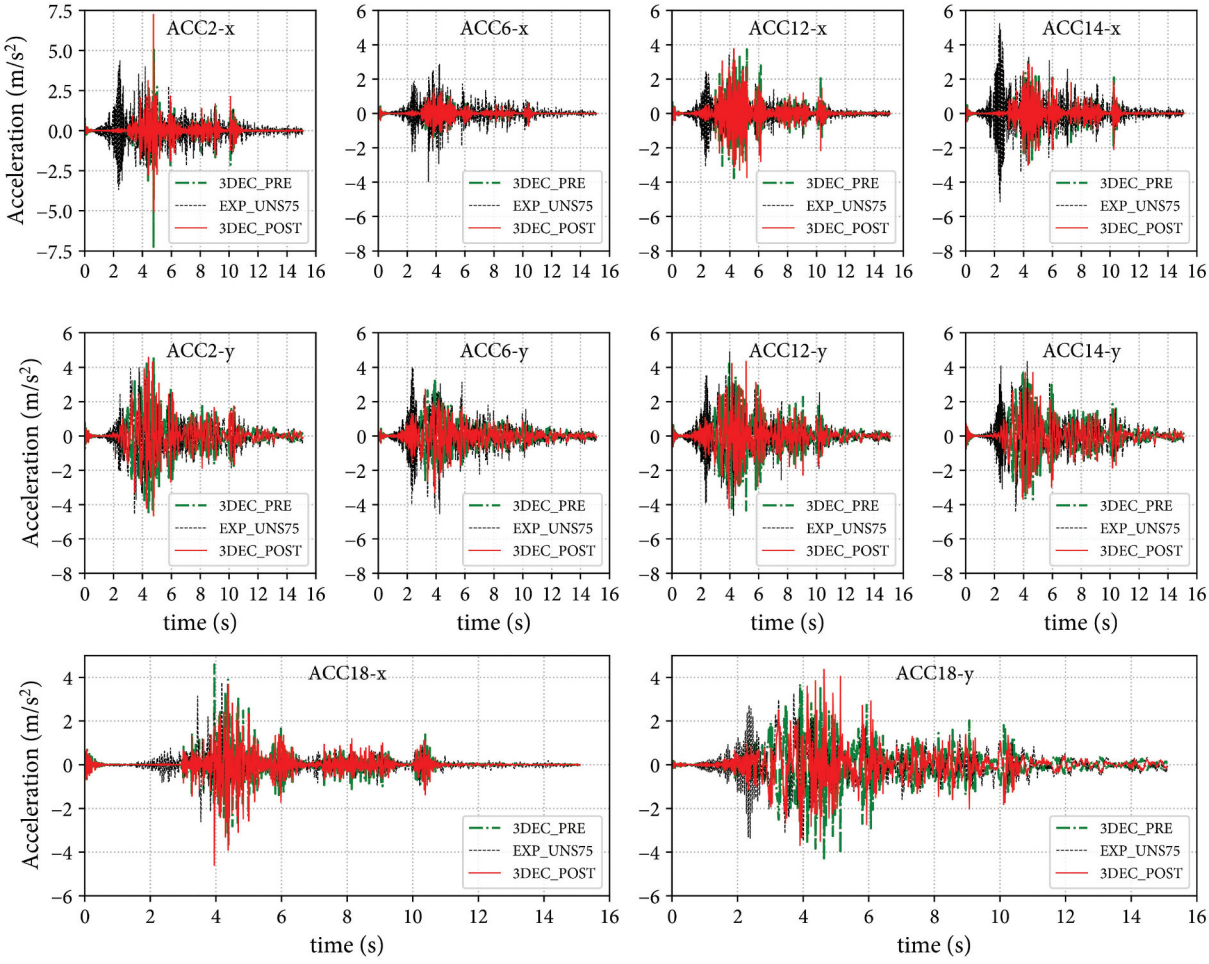

Figure 28. Comparison of post-diction acceleration responses at selected accelerometers on the 75% load increment (unstrengthened case).

considering 15 s of the earthquake signal for the same 100–125–150–175%. In this case, the longer signal could be considered while continuing to prioritize computational effort by using only the signals which accumulated damage. The MAC comparison between the mode shapes from the experimental dynamic identification tests and the numerically predicted mode shapes is presented in Figure 30. While the correlation between numerical and experimental mode shapes is relatively higher for the first mode shapes, it is still below 50%, hence improvement is still needed to find the correlated mode shapes. This will also be considered as a future work of this paper.

The modeling parameters were calibrated to achieve good results in the eigenvalue analysis as well as tested in the dynamic analysis considering non-cumulative damage. In these scenarios, the seismic response of the vault at 150% of the earthquake load was calculated. The results of the non-cumulative analysis displayed a better correlation with experimental results than the prediction phase and were calibrated as well for damping, where mass damping was considered. The mass damping percentage with the best correlation in the non-cumulative damage scenario was the 4% mass damping, which aligned well with the displacements (Figure 31), yet overestimated the acceleration results (maximum relative error of 650%). This can be attributed to a greater level of damage present in the model at this stage. Similar results with 4% mass damping in the cumulative dynamic analysis displayed better results for the accelerations, yet at the end of the seismic load displayed an overestimation of the displacements as well. For this reason, the calibration of the mass damping percentages was chosen at 3% to compare to the experimental results.

In addition, the damage and cracking improved in the post-test numerical model. This model was able to capture the high levels of damage occurring at the movable and fixed piers, as well as the hinge mechanisms in the arch intrados. Diagonal cracks occurred along the arch intrados and extrados at the intersection

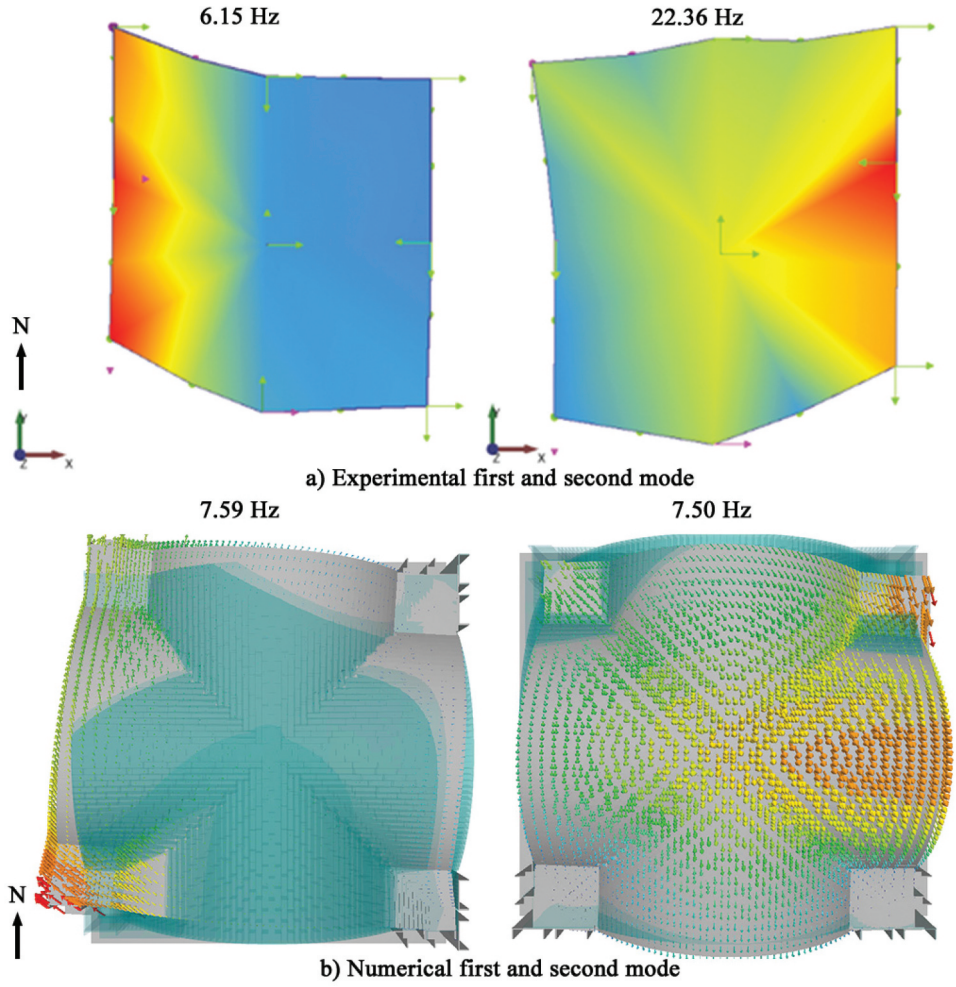

Figure 29. Comparison of eigenvalue analysis and mode shapes for the reinforced numerical model and experiment (strengthened case).

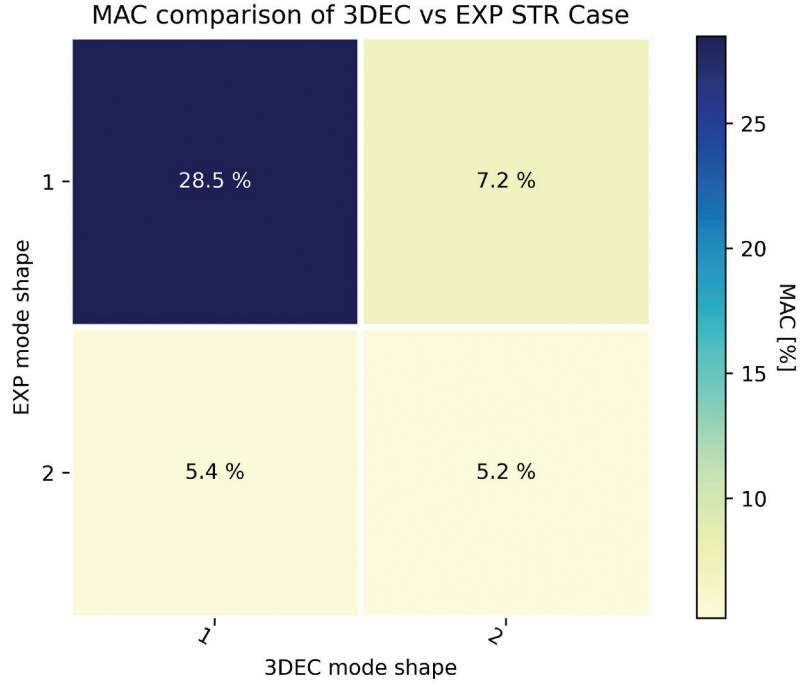

Figure 30. MAC Comparison of 3DEC and EXP for the UNS case.

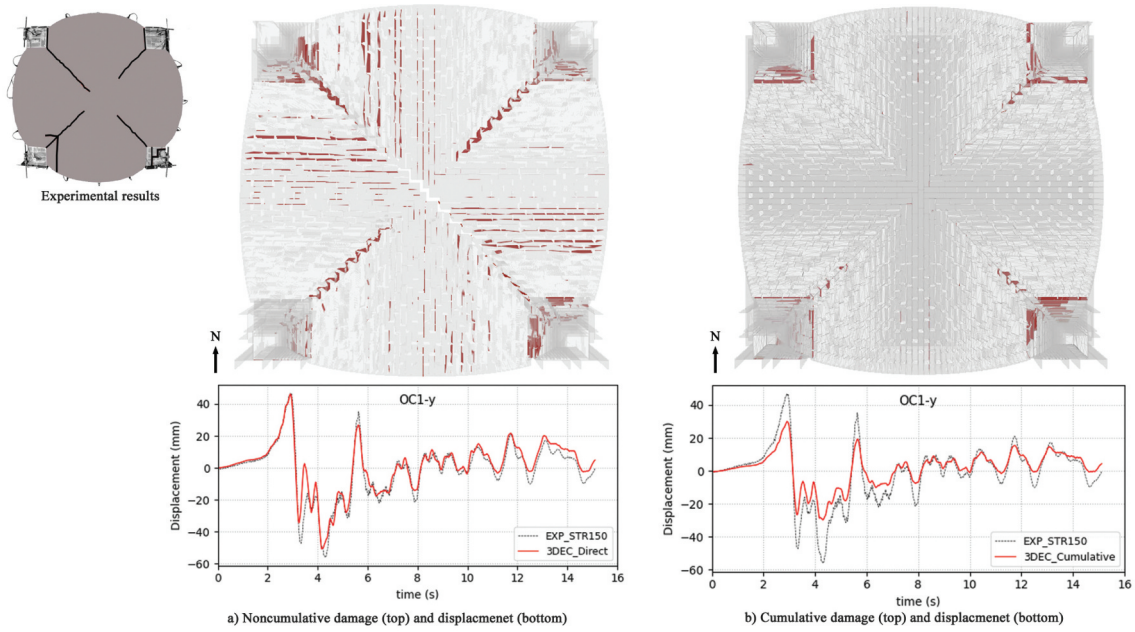

Figure 31. Comparison of cumulative and non-cumulative damage of the strengthened cross vault at the 150% load increment, with the reinforcement hidden.

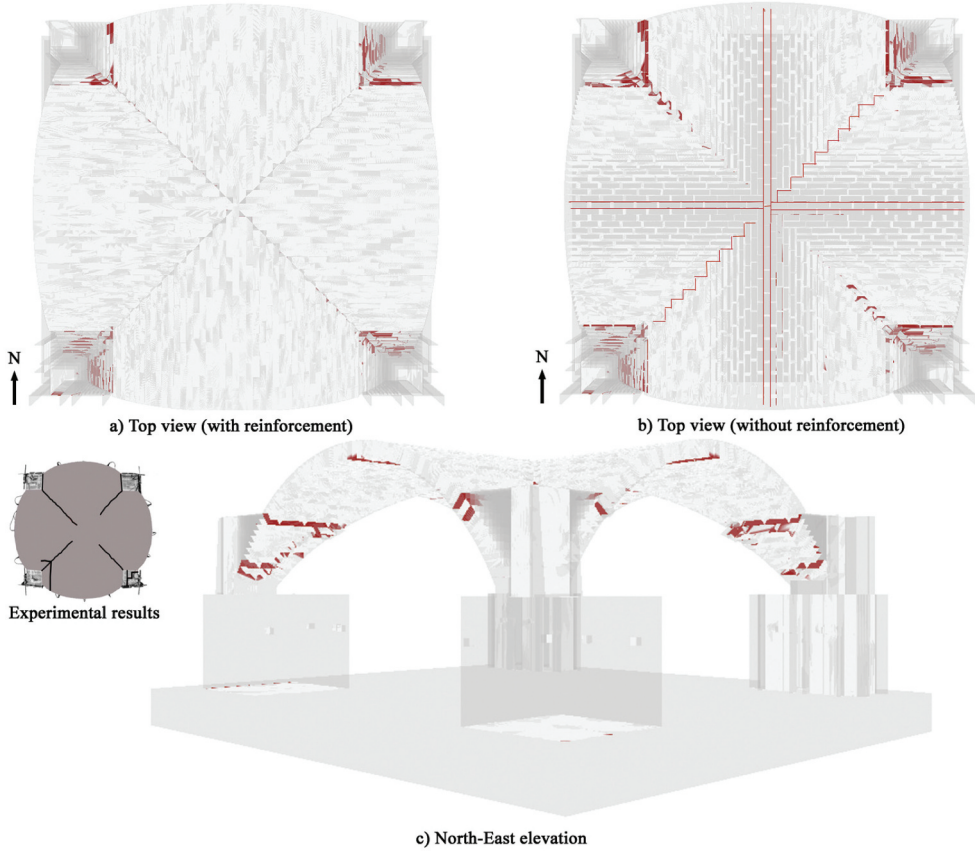

Figure 32. Cumulative damage in the strengthened model at the 150% load increment.

Table 10. Absolute maximum total displacements and acceleration comparison between experiment and post-diction numerical analysis of strengthened case.

		Experimental	Post-diction		Pre-diction	
			Numerical	Relative Error (%)	Numerical	Relative Error (%)
Displacement (mm)	OC1-y	57.21	29.96	−47.6	1.12	−90.7
	OC2-x	39.68	0.30	−99.2	0.59	−98.7
	OC2-y	64.02	29.33	−54.2	2.34	−92.3
	OC4-x	14.38	0.48	−96.7	0.80	−77.3
	OC4-y	62.63	29.47	−52.9	2.26	−82.2
Acceleration (m/s^2)	ACC2-x	10.02	12.7	26.7	9.3	−7.2
	ACC2-y	9.41	11.8	25.4	14.7	56.2
	ACC6-x	11.73	8.8	−25.0	8.8	−25.0
	ACC6-y	9.04	8.8	−2.7	9.2	−1.8
	ACC12-x	9.46	11.6	22.6	11.3	19.5
	ACC12-y	8.35	15.9	90.4	43.2	417.4
	ACC14-x	17.32	7.1	−59.0	12.3	−28.9
	ACC14-y	10.50	10.9	3.8	64.7	518.2
	ACC18-x	8.17	9.6	17.5	4.2	−48.6
	ACC18-y	7.65	9.5	24.2	10.1	32.0

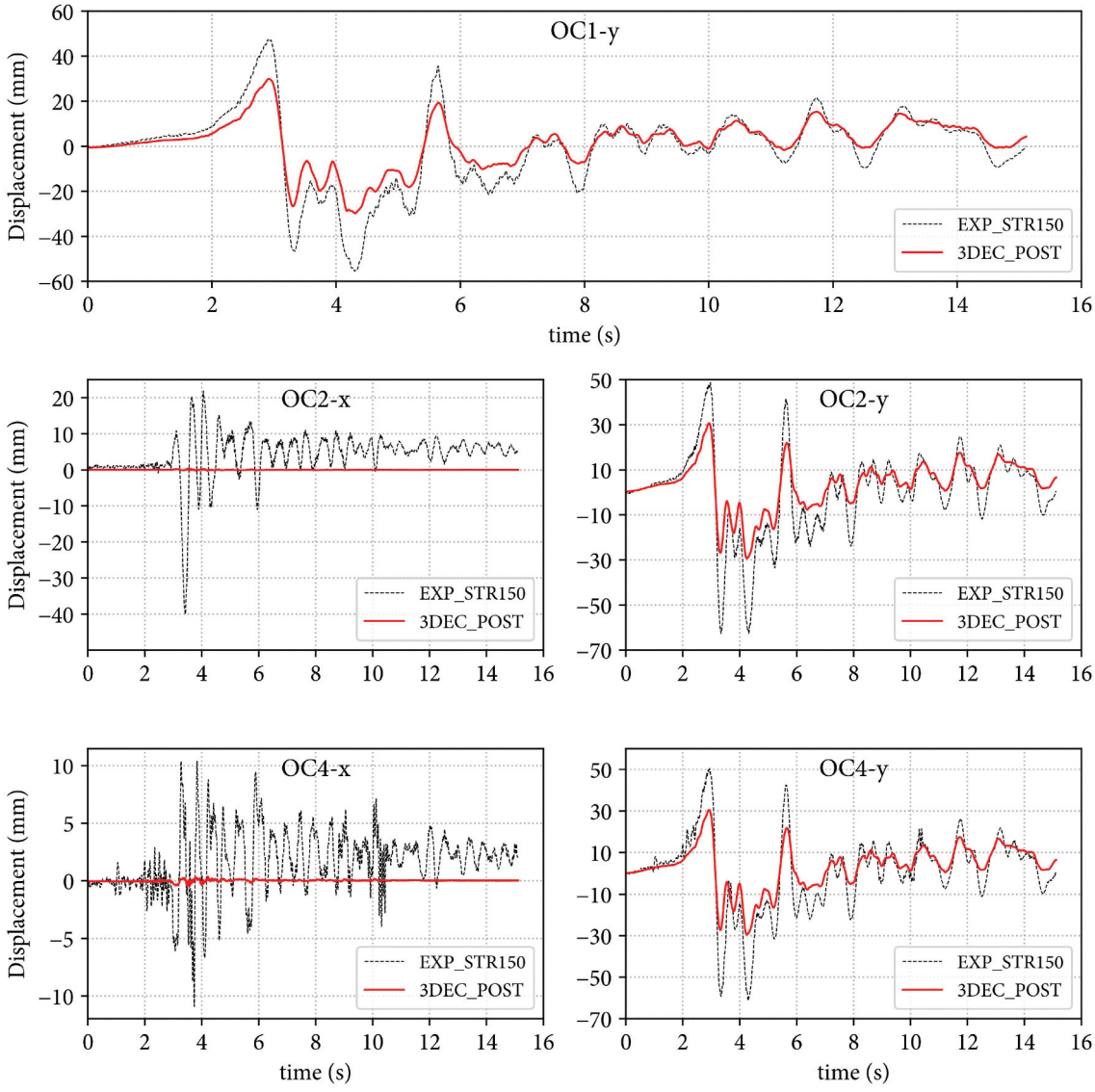

Figure 33. Comparison of displacement responses at each optical cameras on the 150% load increment (strengthened case).

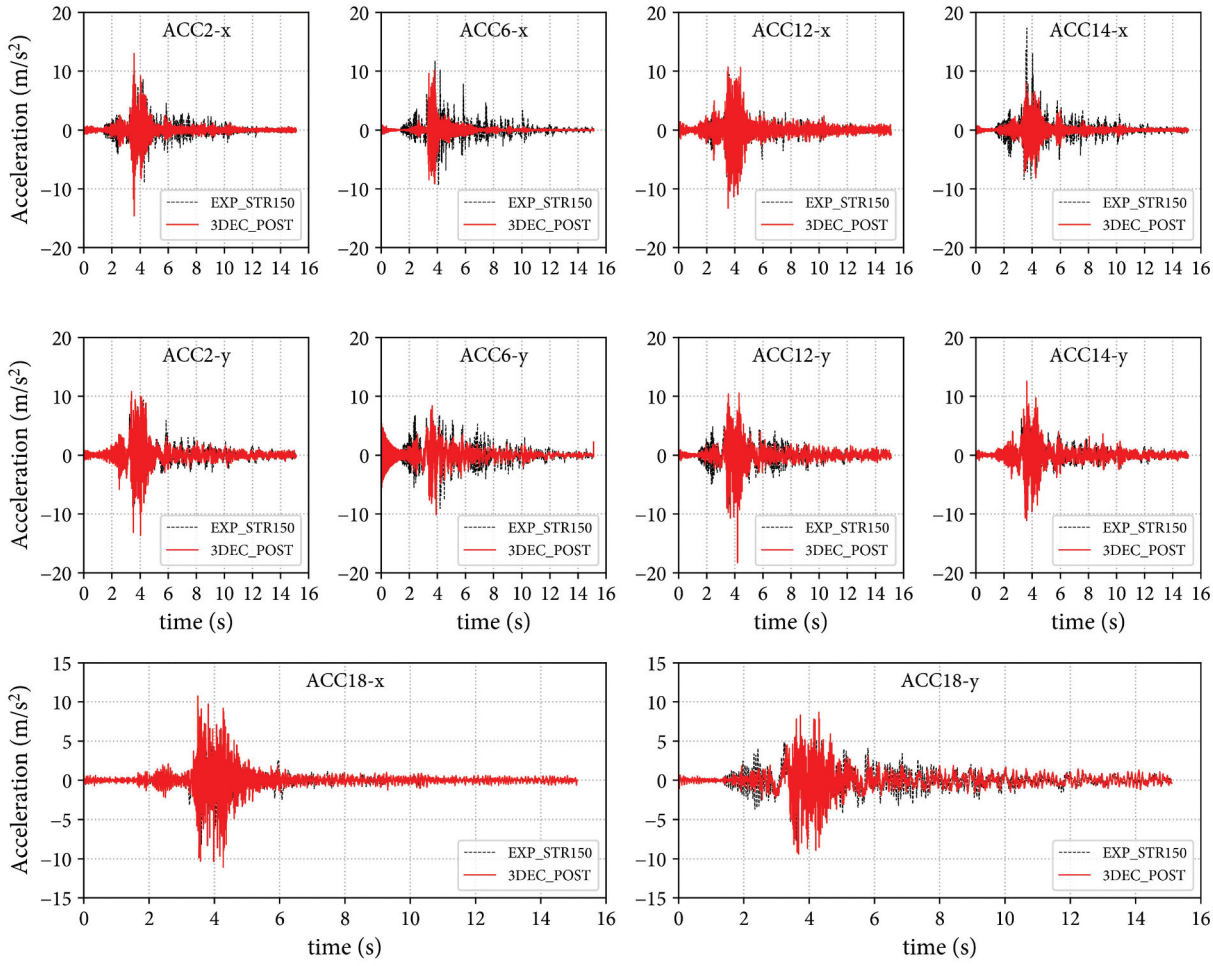

Figure 34. Comparison of post-diction acceleration responses at selected accelerometers on the 150% load increment (strengthened case).

of the cross-vault as well as all the way through bed joints at the center point of each vault portion, as pictured in Figure 32. Limited damage occurred in the reinforcement, with small cracks beginning along the vault diagonals.

5.3.2. Quantitative response comparisons

The improvements in the postdiction phase for the calibration of modeling parameters and damping ratios allowed for an overall improvement in average relative error in the displacement response from 88% in the blind prediction to 70% in the post-diction. For the acceleration, the average relative error in the response decreased from 115% to 29.7%. The absolute maximum displacements of the post-diction numerical model are provided in Table 10 and the corresponding graphs in Figure 33. The difference along the Y-direction remains relatively small in the post-diction, as in the prediction. The better correlation of displacements along the transverse direction can be attributed to the better joint properties between the reinforcement and the vault extrados.

The improvements in the acceleration response in the post-diction model, presented in Table 10, show a better correlation with the experiment in both the longitudinal and transverse directions. This can possibly be attributed to the damping calibration (Figure 34). With further research into the effects of Maxwell damping on the estimation of response, the acceleration responses can be further improved. When compared with the results from the blind prediction (Figure 17), while the displacements are still underestimated, the errors were able to be reduced, in the y-direction especially, throughout the application of the signal.

6. Conclusions

In this paper, a series of numerical analyses were conducted using a three-dimensional distinct element method approach where a masonry cross-vault model

was subjected to uni-directional dynamic excitation. The numerical model served as part of the validation of a shaking-table experiment conducted within the SERA project which was separated into two stages, the blind-prediction and post-diction stages. In the blind-prediction stage, a three-dimensional representation of the cross-vault is created using COMPAS Masonry, an open-source Python-based computational framework for evaluating masonry structures. The geometrical model is then analyzed using the distinct element method (DEM) where masonry blocks are modeled as a system of discrete blocks, interacting at contact points. In DEM, an explicit time-marching integration scheme is utilized to solve the equation of motion of the system. For the masonry part of the vault specimen, the elasto-softening contact model is employed based on the bilinear fracture energy. This contact model is able to model the non-linear behavior of masonry structures through the simulation of crushing, cracking, and sliding failure. The numerical model was tested based on the given information at the prediction stage. In the post-diction phase, the material input parameters, damping ratio, and modeling strategy were calibrated based on the actual experimental data, and the analysis was re-run to better match the experimental results. The model was validated in terms of displacement and acceleration responses, crack pattern, and prediction of natural frequency as well as mode shape during dynamic identification tests. The results of the validation are summarized as follows:

(1) In the prediction stage, the comparison of natural frequency and the first mode shape showed a relatively good agreement between the DEM model and experimental results, where the numerical natural frequency was predicted at 12.5 Hz in comparison to 6.15 Hz from the experimental test. The mode shape comprising shearing movement along the seismic excitation direction was also simulated at the movable piers.

(2) For the unstrengthened case, the displacement response comparison showed that the relative error from the numerical model ranged from 16% to 72%. Similarly, the acceleration response relative error ranges from 2% to 65%. The difference in numerical response was attributed to the non-linearity that was not captured in the numerical model.

(3) For the strengthened case, the displacement response recorded a relative error ranging from 77% to 99% while the error for the acceleration response ranged from 7 to 48 in the X-direction and from 2% to 517% in the Y-direction.

(4) Based on the available experimental data, the material properties were calibrated and the numerical model in the prediction stage was evaluated. Based on the calibration result, it was found that 3% -damping was suitable for the unstrengthened case while 4% -damping was suitable for the strengthened case. An improvement on the modeling strategy was done by detaching the nodes(gridpoints) between the movable piers, steel frame, and shake table element.

(5) In the post-diction stage, the modal analysis showed a better comparison to the numerical model where the numerical first mode natural frequency was predicted at 6.66 Hz, with subsequent mode shapes also predicted relatively well compared to the experimental results.

(6) For the unstrengthened case, the post-diction displacement response showed that the relative error from the numerical model ranged from 12% to 77%. Similarly, the acceleration response relative error ranged from 6% to 67%.

(7) For the strengthened case, the post-diction displacement response recorded a relative error ranging from 47% to 99% while the relative error for the post-diction acceleration response ranged from 17% to 59% in the X-direction and from 2% to 90% in the Y-direction.

(8) It is shown that while the post-diction model is relatively better compared to the prediction model, there were still some discrepancies in terms of the quantitative response. As part of the future work of this paper, a different damping scenario will be considered, such as the use of Maxwell (damping Lemos and Sarhosis (2023)), to better match the experimental response. Furthermore, discretization of the infill pier will also be considered to provide a faithful representation of the experimental specimen.

Acknowledgments

The authors would like to thank Prof Chiara Calderini, Prof Paulo Lourenco, Prof Paulo Candeias, Dr. Michela Rossi, Dr. Nuno Mendes, and Nicoletta Bianchini for images and data related to the LNEC shake table tests. D. Malomo (McGill University) would like to acknowledge the support of the Natural Sciences and Engineering Research Council of Canada (NSERC) [funding reference number RGPIN-2022-03635] and thank Itasca for their support through the Itasca Educational Partnership (IEP) Teaching Program. L. Davis (McGill University) would also like to acknowledge funding received by the Centre d'études interuniversitaire des structures sous charges extrêmes (CEISCE, supported by the Fonds de Recherche du Québec Nature et Technologies).

Disclosure statement

No potential conflict of interest was reported by the author(s).

Funding

This work was supported by the Natural Sciences and Engineering Research Council of Canada [RGPIN-2022-03635]; Centre d'études interuniversitaire des structures sous charges extrêmes.

ORCID

Y.P. Oktiovan http://orcid.org/0000-0001-9660-1932
L. Davis http://orcid.org/0000-0002-9974-7619
R. Wilson http://orcid.org/0000-0003-1171-2110
A. Dell'Endice http://orcid.org/0000-0002-4799-6015
A. Mehrotra http://orcid.org/0000-0002-3453-2879
B. Pulatsu http://orcid.org/0000-0002-7040-0734
D. Malomo http://orcid.org/0000-0002-4518-5841

Data availability statement

The data that support the findings of this study are available from the corresponding author, Y. P. Oktiovan, upon reasonable request.

References

Angjeliu, G., G. Cardani, and D. Coronelli. 2019. A parametric model for ribbed masonry vaults. *Automation in Construction* 105:102785. doi:10.1016/j.autcon.2019.03.006.

Augenti, N., and F. Parisi. 2010. Learning from construction failures due to the 2009 L'Aquila, Italy, earthquake. *Journal of Performance of Constructed Facilities* 24 (6):536–55. doi:10.1061/(ASCE)CF.1943-5509.0000122.

Barentin, C., T. V. M. Cristián, and P. Block. 2018. Robotically controlled scale-model testing of masonry vault collapse. *Meccanica* 53 (7):1917–29. doi:10.1007/s11012-017-0762-6.

Bejarano-Urrego, L., E. Verstrynge, G. Giardina, and K. Van Balen. 2018. Crack growth in masonry: Numerical analysis and sensitivity study for discrete and smeared crack modelling. *Engineering Structures* 165:471–85. doi:10.1016/j.engstruct.2018.03.030.

Bertolesi, E., J. M. Adam, P. Rinaudo, and P. A. Calderón. 2019. Research and practice on masonry cross vaults – a review. *Engineering Structures* 180:67–88. doi:10.1016/j.engstruct.2018.10.085.

Bianchini, N., C. Calderini, N. Mendes, P. Candeias, and P. B. Lourenço. 2023. *Blind prediction competition - sera. Ta - seismic response of masonry cross vaults: Shaking table tests and numerical validations* (Version 1). Zenodo. doi:10.5281/zenodo.7624666.

Bianchini, N., N. Mendes, C. Calderini, P. Candeias, M. Rossi, and P. B. Lourenço. 2022. Seismic response of a small-scale masonry groin vault: Experimental investigation by performing quasi-static and shake table tests. *Bulletin of Earthquake Engineering* 20 (3):1739–65. https://link.springer.com/article/10.1007/s10518-021-01280-0.

Bianchini, N., N. Mendes, P. B. Lourenço, C. Calderini, and M. Rossi. 2019. Seismic assessment of masonry cross vaults through numerical nonlinear static and dynamic analysis. *COMPDYN*, Eccomas Proceedia. www.eccomasproceedia.org .

Block, P., and L. Lachauer. 2013. Three-dimensional (3D) equilibrium analysis of gothic masonry vaults. *International Journal of Architectural Heritage* 8 (3):312–35. doi:10.1080/15583058.2013.826301.

Bui, T.-T., A. Limam, and V. Sarhosis. 2021. Failure analysis of masonry wall panels subjected to in-plane and out-of-plane loading using the discrete element method. *European Journal of Environmental and Civil Engineering*. 25 (5):876–92. doi:10.1080/19648189.2018.1552897.

Cannizzaro, F., B. Pantò, S. Caddemi, and I. Caliò. 2018. A discrete macro-element method (DMEM) for the non-linear structural assessment of masonry arches. *Engineering Structures* 168:243–56. doi:10.1016/j.engstruct.2018.04.006.

Carfagnini, C., S. Baraccani, S. Silvestri, and D. Theodossopoulos. 2018. The effects of in-plane shear displacements at the springings of gothic cross vaults. *Construction and Building Materials* 186:219–32. doi:10.1016/j.conbuildmat.2018.07.055.

Chen, S., A. Ferrante, F. Clementi, and K. Bagi. 2021. DEM analysis of the effect of bond pattern on the load bearing capacity of barrel vaults under vertical loads. *International Journal of Masonry Research and Innovation* 6 (3):346–73. doi:10.1504/IJMRI.2021.116234.

Cundall, P. A. 1971. A Computer Model for Simulating Progressive Large Scale Movements in Blocky Rock Systems. *Proceedings of the Symposium of the International Society for Rock Mechanics*, France 8:129–46. Society for Rock Mechanics (ISRM).

Cundall, P. A. 1982. Adaptive density-scaling for time-explicit calculations. In *Proceedings of the 4th International Conference on Numerical Methods in Geomechanics*, Edmonton, Canada 1:23–26.

Cundall, P. A. 1988. Formulation of a three-dimensional distinct element model—part I. A scheme to detect and represent contacts in a system composed of many polyhedral blocks. *International Journal of Rock Mechanics and Mining Sciences & Geomechanics Abstracts* 25 (3):107–16. https://www.sciencedirect.com/science/article/pii/0148906288922930.

D'Altri, A. M., G. Castellazzi, S. de Miranda, and A. Tralli. 2017. Seismic-induced damage in historical masonry vaults: A case-study in the 2012 Emilia earthquake-stricken area. *Journal of Building Engineering* 13:224–43. doi:10.1016/j.jobe.2017.08.005.

Dell'endice, A. 2022. Structural Assessment and Design of Unreinforced Masonry Structures using Discrete Element Modelling. PhD diss., ETH Zurich. 10.3929/ETHZ-B-000596377.

Dell'endice, A., M. J. DeJong, T. Van Mele, and P. Block. 2022. Structural analysis of unreinforced masonry spiral staircases using discrete element modelling. *Structures* 46:214–32. doi:10.1016/j.istruc.2022.10.070.

Dell'endice, A., A. Iannuzzo, M. J. DeJong, T. Van Mele, and P. Block. 2021. Modelling imperfections in unreinforced masonry structures: Discrete element simulations and scale model experiments of a pavilion vault. *Engineering Structures* 228:111499. doi:10.1016/j.engstruct.2020.111499.

Foti, D., V. Vacca, and I. Facchini. 2018. DEM modeling and experimental analysis of the static behavior of a dry-joints masonry cross vaults. *Construction and Building Materials* 170:111–20. doi:10.1016/j.conbuildmat.2018.02.202.

Gaetani, A. 2020. Seismic Performance of Masonry Cross Vaults: Learning from historical developments and experimental testing. PhD diss., Sapienza University, Rome.

Galvez, F., D. Dizhur, and J. M. Ingham2023. Adjacent interacting masonry structures: Shake table test blind prediction discrete element method simulation. *Bulletin of Earthquake Engineering*. doi:10.1007/s10518-023-01640-y.

Galvez, F., L. Sorrentino, D. Dizhur, and J. M. Ingham. 2021. Using DEM to investigate boundary conditions for rocking URM facades subjected to earthquake motion. *Journal of Structural Engineering (United States)* 147(11). doi:10.1061/(ASCE)ST.1943-541X.0003171.

Grillanda, N., A. Chiozzi, G. Milani, and A. Tralli. 2019. Collapse behavior of masonry domes under seismic loads: An adaptive NURBS kinematic limit analysis approach. *Engineering Structures* 200:109517. doi:10.1016/j.engstruct.2019.109517.

Hall, J. F. 2006. Problems encountered from the use (or misuse) of Rayleigh damping. *Earthquake Engineering & Structural Dynamics* 35 (5):525–45. doi:10.1002/eqe.541.

Hart, R., P. A. Cundall, and J. V. Lemos. 1988. Formulation of a three-dimensional distinct element model—part II. Mechanical calculations for motion and interaction of a system composed of many polyhedral blocks. In *International journal of rock mechanics and mining sciences & geomechanics abstracts*, 117–25. Elsevier.

Iannuzzo, A., A. Dell'endice, R. Avelino, G. Kao, T. Van Mele, and P. Block. 2021. COMPAS masonry: A computational framework for practical assessment of unreinforced masonry structures. *Proceedings of the 12th International Conference on Structural Analysis of Historical Constructions (SAHC 2020)*, Barcelona, 1882–92.

Itasca Consulting Group Inc. 2013. *3DEC three dimensional distinct element code*. Minneapolis, Minnesota: Itasca Consulting Group.

Lemos, J. V. 2007. Discrete element modeling of masonry structures. *International Journal of Architectural Heritage* 1 (2):190–213. doi:10.1080/15583050601176868.

Lemos, J. V. 2008. Block modelling of rock masses. *European Journal of Environmental and Civil Engineering* 12 (7–8):915–49. doi:10.1080/19648189.2008.9693054.

Lemos, J. V., and V. Sarhosis. 2023. Dynamic analysis of masonry arches using Maxwell damping. *Structures* 49:583–92. doi:10.1016/j.istruc.2023.01.139.

Lengyel, G., and K. Bagi. 2015. Numerical analysis of the mechanical role of the ribs in groin vaults. *Computers & Structures* 158:42–60. doi:10.1016/j.compstruc.2015.05.032.

Lengyel, G., and R. Károly Németh. 2018. The mechanical behavior of ribs in masonry groin vaults subjected to seismic load. *International Journal of Architectural Heritage* 13 (6):886–900. doi:10.1080/15583058.2018.1491652.

Lourenço, P. B. 1996. Computational Strategies for Masonry Structures. Doctoral Thesis, Delft University.

Lourenço, P. B. 2010. Recent advances in masonry modelling: Micromodelling and homogenisation. *Multiscale Modeling in Solid Mechanics: Computational Approaches* 3:251–294. doi:10.1142/9781848163089_0006.

Lourenço, P. B., J. G. Rots, and J. Blaauwendraad. 1995. Two approaches for the analysis of masonry structures: Micro and macro-modeling. *HERON* 40 (4):313–340.

Malomo, D., and M. J. DeJong. 2022. M-DEM simulation of seismic pounding between adjacent masonry structures. *Bulletin of Earthquake Engineering* 1–26. doi:10.1007/s10518-022-01545-2.

Malomo, D., M. J. DeJong, and A. Penna. 2021. Influence of bond pattern on the in-plane behavior of URM piers. *International Journal of Architectural Heritage* 15 (10):1492–511. https://www.tandfonline.com/action/journalInformation?journalCode=uarc20.

McInerney, J., and M. J. DeJong. 2015. Discrete element modeling of groin vault displacement capacity. *International Journal of Architectural Heritage* 9 (8):1037–49. doi:10.1080/15583058.2014.923953.

Meriggi, P., G. de Felice, S. De Santis, F. Gobbin, A. Mordanova, and B. Pantò. 2019. Distinct Element Modelling of Masonry Walls under Out-Of-Plane Seismic Loading. *International Journal of Architectural Heritage*. 13 (7):1110–23. doi:10.1080/15583058.2019.1615152.

Milani, G., M. Rossi, C. Calderini, and S. Lagomarsino. 2016. Tilting plane tests on a small-scale masonry cross vault: Experimental results and numerical simulations through a heterogeneous approach. *Engineering Structures* 123:300–12. doi:10.1016/j.engstruct.2016.05.017.

Nodargi, N. A., and P. Bisegna. 2022. A finite difference method for the static limit analysis of masonry domes under seismic loads. *Meccanica* 57 (1):121–41. doi:10.1007/s11012-021-01414-3.

Paris, V., A. Pizzigoni, and S. Adriaenssens. 2020. Statics of self-balancing masonry domes constructed with a cross-herringbone spiraling pattern. *Engineering Structures* 215:110440. doi:10.1016/j.engstruct.2020.110440.

Pastor, M., M. Binda, and T. Harčarik. 2012. Modal assurance criterion. *Procedia Engineering* 48:543–48. doi:10.1016/j.proeng.2012.09.551.

Pluijm van der, R. 1997. Non-linear behaviour of masonry under tension. *Heron* 42 (1):25–54.

Pulatsu, B. 2023. Coupled elasto-softening contact models in DEM to predict the in-plane response of masonry walls. *Computational Particle Mechanics* 10 (6):1759–70. https://link.springer.com/10.1007/s40571-023-00586-x.

Pulatsu, B., E. Erdogmus, P. B. Lourenço, J. V. Lemos, and J. Hazzard. 2020. Discontinuum analysis of the fracture mechanism in masonry prisms and wallettes via discrete element method. *Meccanica* 55 (3):505–23. doi:10.1007/s11012-020-01133-1.

Pulatsu, B., E. Erdogmus, P. B. Lourenço, J. V. Lemos, and K. Tuncay. 2020. Simulation of the in-plane structural behavior of unreinforced masonry walls and buildings using DEM. In *Structures*, Vol. 27, 2274–87. doi:10.1016/j.istruc.2020.08.026.

Pulatsu, B., E. Erdogmus, P. B. Lourenço, and R. Quey. 2019. Simulation of uniaxial tensile behavior of quasi-brittle materials using softening contact models in DEM. *International Journal of Fracture* 217 (1–2):105–25. doi:10.1007/s10704-019-00373-x.

Pulatsu, B., S. Gonen, and P. B. Lourenço. 2021. Static and impact response of a single-span stone masonry arch. *Infrastructures*. 6(12):178. Cited by: 4; All Open Access, Gold Open Access, Green Open Access. doi:10.3390.

Rossi, M., C. Calderini, and S. Lagomarsino. 2016. Experimental testing of the seismic in-plane displacement capacity of masonry cross vaults through a scale model. *Bulletin of Earthquake Engineering* 14 (1):261–81. doi:10.1007/s10518-015-9815-1.

Seismosoft. 2002. SeismoSignal - a computer program for signal processing of time-histories. http://www.seismosoft.com/.

Simon, J., and K. Bagi. 2016. Discrete element analysis of the minimum thickness of oval masonry domes. *International Journal of Architectural Heritage* 10 (4):457–75. doi:10.1080/15583058.2014.996921.

Szabó, S., M. Francesco Funari, B. Pulatsu, and P. B. Lourenço. 2022. Lateral capacity of URM walls: A parametric study using macro and micro limit analysis predictions. *Applied Sciences* 12 (21):10834. doi:10.3390/app122110834.

Tóth, A. R., Z. Orbán, and K. Bagi. 2009. Discrete element analysis of a stone masonry arch. *Mechanics Research Communications* 36 (4):469–80. doi:10.1016/j.mechrescom.2009.01.001.

Van Mele, T. 2022. *BlockResearchgroup/compas-masonry: COMPAS masonry alpha* (v0.1.0). Zenodo. doi:10.5281/zenodo.6044225.

Van Mele, T., A. Liew, T. Mendez, and M. Rippmann. ETHZ: Block Research Group. 2017. Zurich, Switzerland: Block Research Group. http://compas-dev.github.io/compas/